OPTIMIZATION OF FLOW CONDITIONS AND INVESTIGATION OF CRYSTALLIZATION KINETICS FROM A SUPERSATURATED SOLUTION IN A TWO-PHASE MICROFLUIDIC SYSTEM

İKİ-FAZLI BİR MİKRO-AKIŞKAN SİSTEMDE AKIŞ KOŞULLARININ OPTİMİZASYONU VE AŞIRI DOYGUN BİR ÇÖZELTİDE KRİSTALLEŞME KİNETİĞİNİN İNCELENMESİ

TIJANI AHMED AHMED

ASSOC. PROF. DR. SELİS ÖNEL

Supervisor

Submitted to

Graduate Schoolof Science and Engineering of Hacettepe University

as a Partial Fulfilment to the Requirements

for the Award of Degree of Master of Science

in Chemial Engineering.

2022

ABSTRACT

OPTIMIZATION OF FLOW CONDITIONS AND INVESTIGATION OF CRYSTALLIZATION KINETICS FROM A SUPERSATURATED SOLUTION IN A TWO-PHASE MICROFLUIDIC SYSTEM

Tijani Ahmed AHMED

Master of Science, Department of Chemical Engineering

Supervisor: Assoc. Prof. Dr. Selis ÖNEL

August 2022, 73 pages

The effects of thermodynamic conditions on the kinetics of nucleation from supersaturated solutions have been of great interest in controlling the synthesis of nano/micro particles with advanced physical, chemical, and optical properties. Microfluidic systems offer a medium, where the nucleation phenomena can be better controlled and examined. This study is aimed at optimization of two-phase flow conditions for producing uniform picoreactors in a microfluidic system and investigation of the thermal conditions for nucleation from a supersaturated solution. The microfluidic system consists of an x-channel for the formation of droplets followed by a serpentine channel integrated with a temperature controlled transparent heater. The solution contains zirconium chloride ($ZrCl_4$) and 1,4-benzenedicarboxylic acid (BDC) dissolved in N,N-

dimethylformamide (DMF), i.e. a precursor solution for the synthesis of UiO-66 crytals with a metal organic framework (MOF) structure. The precursor solution, as the dispersed phase, and silicone oil, as the continuous phase, were used to form monodispersed spherical picoliter reactors that travelled with equal interdroplet distances in the microfluidic system. The desired size of the droplets was optimized by varying the ratio of the flow rates of the dispersed and the continuous phases, Qd/Qc. The reduction in Qd/Qc caused droplets to be smaller and more spherical. At the optimized condition, where Qd/Qc was 0.05, the average diameter of the droplets was 105.23±5 μm reducing to 70±3 μm just before they entered the serpentine, losing about 30 % of the size. Shrinkage of the droplets, due to the dissolution of the solvent into the oil causing supersaturation of the precursor solution, continued in the hot region of the device until nucleation started.

Crystallization experiments were carried out at 50, 80 and 100 ^{o}C to determine the initial point and the rate of nucleation based on temperature and picoreactor (droplet) size. Initial point of nucleation gave the residence time of the droplet in the heated serpentine region until nucleation took place in the droplet. The rate of nucleation was determined by counting the number of droplets with nuclei over time. The size of the droplets affected the nucleation time as smaller droplets had nucleation earlier at the same temperature. For the case of 80 ^{o}C, the 70 μm droplets nucleated at 30 ±5 seconds, while the 90 ±5 and 110 ±5 μm droplets nucleated at 109 ±3 and 112 ±5 seconds, respectively. The generation of supersaturation in the droplets due to shrinkage drove the nucleation earlier at higher temperatures resulting with more droplets nucleated. This scenario followed Lamer's model of instantaneous nucleation. Kinetic rate constants for nucleation, k_N, were calculated using the classical nucleation theory as 0.0003175 s^{-1}, 0.0156 s^{-1}, and 0.1174 s^{-1} for 50, 80, and 100 ^{o}C respectively. The activation energy for nucleation was found as 119 $kJmol^{-1}$. XRD analyses of the synthesized particles showed a positive influence of higher temperatures within the range applied confirming the potential of the microfluidic system to carry out crystallization from supersaturated solutions.

Keywords: Nucleation kinetics, two-phase microfluidic system, supersaturated solution crystallization, picoreactor

ÖZET

İKİ FAZLI BİR MİKRO-AKIŞKAN SİSTEMDE AKIŞ KOŞULLARININ OPTİMİZASYONU VE AŞIRI DOYGUN BİR ÇÖZELTİDE KRİSTALLEŞME KİNETİĞİNİN İNCELENMESİ

Tijani Ahmed AHMED

Yüksek Lisans, Kimya Mühendisliği Bölümü

Tez Danışmanı: Doç. Dr. Selis ÖNEL

Ağustos 2022, 73 sayfa

Termodinamik koşulların aşırı doymuş çözeltilerde çekirdeklenme kinetiği üzerindeki etkileri ileri fiziksel, kimyasal ve optik özelliklere sahip nano/mikro parçacıkların kontrollü bir şekilde sentezinde büyük önem taşımaktadır. Mikroakışkan sistemler, ısı ve kütle aktarım olaylarının çok daha hızlı ilerleyebildiği ve çekirdeklenme olaylarının daha iyi kontrol edilip incelenebileceği bir ortam sunmaktadır. Bu çalışmada, mikroakışkan bir sistemde eş boyutlu pikoreaktörler üretmek için iki fazlı akış koşullarının optimizasyonu ve aşırı doymuş bir çözeltide çekirdeklenme için ısıl koşulların incelenmesi amaçlanmaktadır. Mikroakışkan sistem, şekilde görüldüğü gibi damlacık oluşumu için bir x-kavşaklı kanal ve onu takip eden kısımda sıcaklık kontrollü saydam bir ısıtıcı ile entegre edilmiş bir serpantin kanalından oluşmaktadır. Bu cihaz daha önceki bir araştırma için tez danışmanı Doç. Dr. Selis Önel tarafından tasarlanmış ve üretilmiştir.

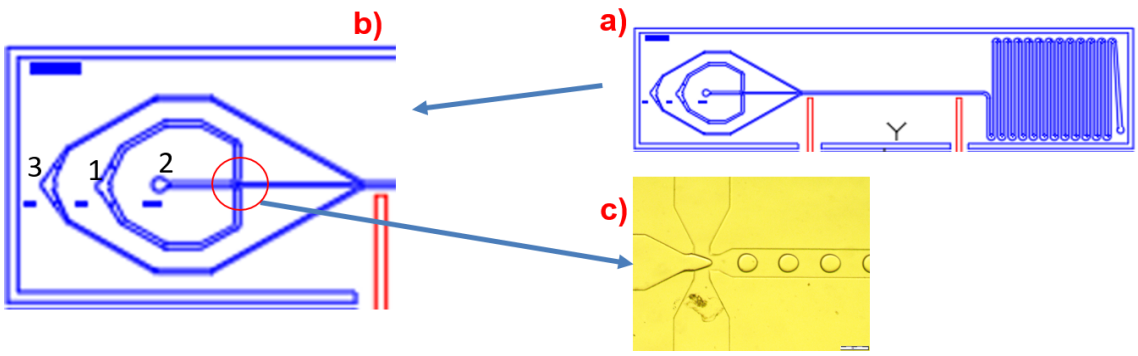

Şekil 1. Çalışmada kullanılan ve tez danışmanı Dr. Selis Önel tarafından tasarlanan ısıl mikroakışkan sistemin a) genel görünümü, b) x-kavşak ve giriş noktaları ve c) x-kavşakta damlacık oluşumunun mikroskop görüntüsü.

Çalışmada kristalleşmenin incelenmesi için kullanılan aşırı doygun çözelti N,N-dimetilformamid (DMF) içinde çözülmüş zirkonyum klorür (ZrCl4) ve 1,4-benzendikarboksilik asit (BDC), yani metal organik çerçeve (metal organic framework, MOF) yapısına sahip UiO-66 kristallerinin sentezi için kullanılan bir öncü çözeltidir. Çözelti reçetesi Prof. Dr. Burcu Akata Kurç'un (ODTÜ Mikro ve Nano Teknoloji Programı) laboratuvarından temin edilmiştir.

Mikroakışkan sistemde eşit damlacıklar arası mesafelerle hareket eden eş boyutlu küresel pikolitre reaktörleri oluşturmak için dağınık faz olarak öncü çözelti ve sürekli faz olarak silikon yağı kullanılmıştır. Damlacıkların istenen boyutu, dağınık ve sürekli fazların akış hızlarının oranı Qd/Qc değiştirilerek optimize edilmiştir. Qd/Qc'deki azalma, damlacıkların daha küçük ve daha küresel olmasına neden olmuştur. Qd/Qc'nin 0.05 olduğu optimize edilmiş durumda, damlacıkların ortalama çapının 105.23±5 µm olduğu ölçülmüştür. X-kavşak sonrası kanalda ilerleyen damlacıkların boyutunun serpantine girmeden hemen önce 70±3 µm'ye düştüğü ve damlacıkların boyut bazında yaklaşık %30 küçüldüğü görülmüştür. Öncü çözelti içindeki hangi maddenin yağ içinde çözündüğünün anlaşılması için silikon yağı ayrı ayrı BDC+DMF çözeltisi, $ZrCl_4$+DMF çözeltisi ve saf DMF ile oda sıcaklığında karıştırılarak emülsiyonlar oluşturulmuştur. Her sistem için cam lam üzerinde damlacıkların boyutu incelenmiştir. DMF'in Şekil 2'de görüldüğü gibi yağ içinde çözüldüğü ve bu nedenle damlacık içindeki çözeltinin aşırı doygun hale geldiği anlaşılmıştır.

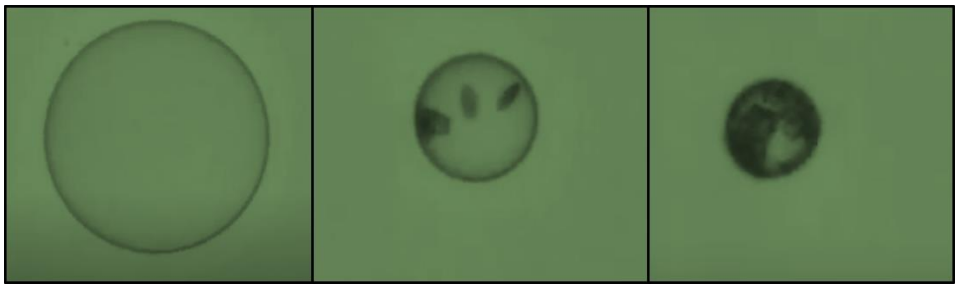

Şekil 2. DMF çözücüsünün silikon yağına geçmesi sonucu öncü çözelti damlacığının küçülmesi, derişiminin artması sonucu aşırı doygun hale gelmesi ve kristalleşmenin başlaması.

Damlacıkların küçülme hızı, damlacıklar mikroakışkan cihazın ısıtılan bölgesine girdikten sonra artarak çekirdeklenme başlayana kadar devam etmektedir. Çekirdeklenme başlangıç noktası ve hızının farklı pikoreaktör boyutu ve sıcaklık koşullarında nasıl değiştiğini belirlemek amacıyla: 1. sıcaklık sabit tutulup damlacık boyutu değiştirilerek ve 2. damlacık boyutu sabit tutulup sıcaklık değiştirilerek deneyler yapılmıştır. Sabit 80 °C sıcaklıkta 70 µm, 90 µm ve 110 µm çapa sahip damlacıklarda serpantin kanalında çekirdeklenmenin başladığı noktalar Şekil 3'te temsili olarak gösterilmiştir.

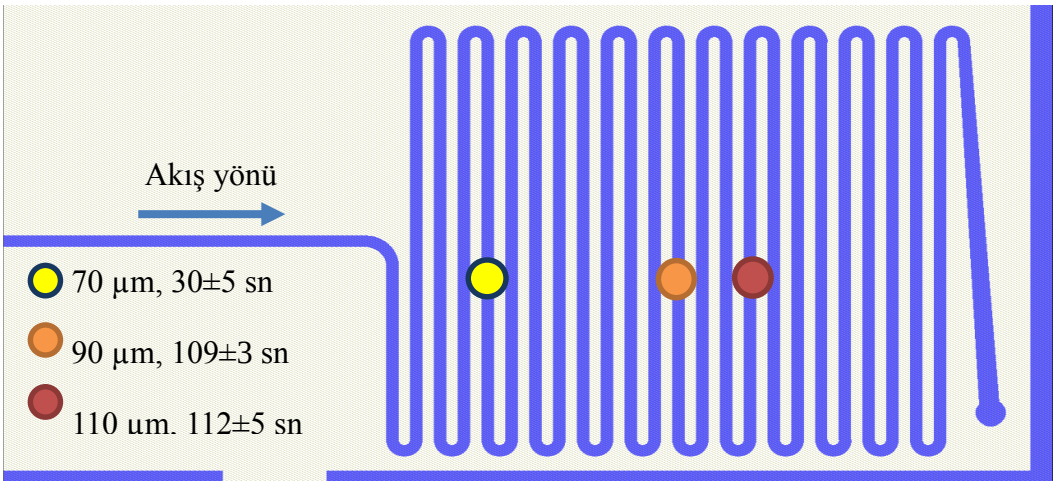

Şekil 3. UiO-66 öncü çözeltisi içeren 70 µm, 90 µm ve 110 µm çapa sahip damlacıklarda sabit 80 °C sıcaklıkta çekirdeklenme süresinin ve çekirdeklenmenin serpantin kanalda hangi noktada başladığının temsili gösterimi.

Reaktör ya da damlacık boyutunun küçülmesinin kristallenmeyi hızlandırdığı görülmüştür. Damlacık boyutu 70 µm'de sabit tutularak 50 °C, 80 °C ve 100 °C'de

sıcaklık etkisini görmek amacıyla yapılan deneylerde damlacıklarda serpantin kanalında çekirdeklenmenin başladığı süreler ve bu sürelere tekabül eden noktalar Şekil 4'te temsili olarak gösterilmiştir.

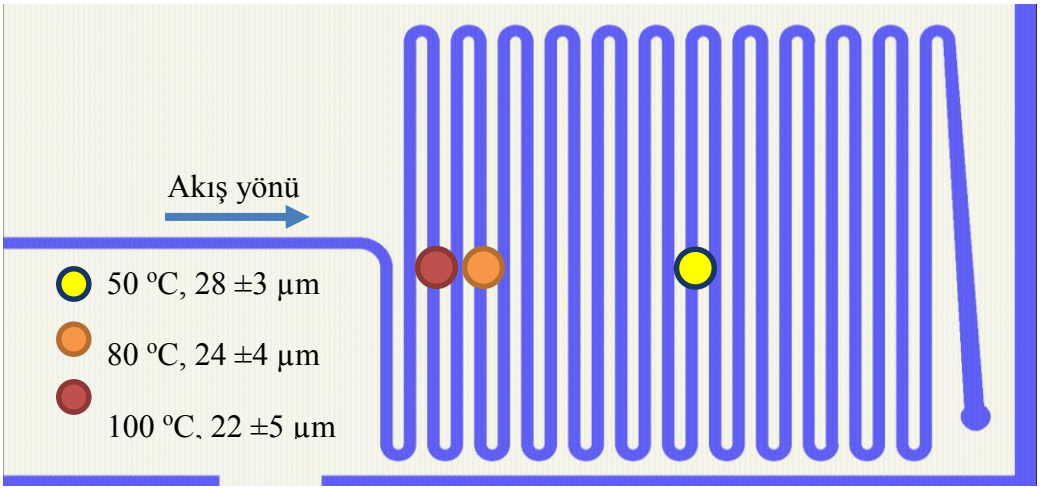

Şekil 4. UiO-66 öncü çözeltisi içeren 70 µm başlangıç çapına sahip damlacıkların 50 °C, 80 °C ve 100 °C'de serpantin kanala girdikten sonra çekirdeklenmeden hemen önceki boyutları ve çekirdeklenmenin serpantin kanalda hangi noktada başladığının temsili gösterimi.

Çekirdeklenmenin başlangıç noktasının mikroakışkan sistemdeki deneylerle belirlenebilmesi, damlacığın çekirdeklenme gerçekleşene kadar ısıtılmış serpantin bölgesinde kalma süresinin belirlenebilmesi sağlamıştır. Çekirdeklenme hızı, çekirdekli damlacıkların sayısı zamana bağlı olarak sayılarak belirlenmiştir. Çekirdeklenme aynı sıcaklık koşullarında daha küçük damlacıklarda daha erken gerçekleştiğinden, damlacıkların boyutu çekirdeklenme süresini etkilemiştir. Sabit 80 °C'de, 70 µm'lik damlacıklar 30±5 saniyede çekirdeklenirken, 90±5 ve 110±5 µm'lik damlacıklar sırasıyla 109±3 ve 112±5 saniyede çekirdeklenmiştir. Çözücünün silikon yağına geçmesi ile damlacıkların küçülmesi ve aşırı doygun hale gelmesi, çekirdeklenmenin sıcaklık yüksekdikçe daha erken başlamasına ve bu da daha fçok sayıda damlacığın çekirdeklenmesine neden olmuştur. Bu senaryo, Lamer'in anlık çekirdeklenme modelini izlemektedir.

Çekirdeklenme için kinetik hız sabitleri, k_N, klasik çekirdeklenme teorisi kullanılarak 50 °C, 80 °C ve 100 °C için sırasıyla 0,0003175 sn^{-1}, 0,0156 sn^{-1} ve 0,1174 sn^{-1} olarak hesaplanmıştır. Çekirdeklenme için aktivasyon enerjisi 119 kJ/mol olarak bulunmuştur. Sentezlenen parçacıkların XRD analizleri, mikroakışkan sistemin aşırı doymuş çözeltilerden kristalizasyon gerçekleştirme potansiyelini doğrulamıştır ve uygulanan aralık içinde daha yüksek sıcaklıkların kristalleşme üzerinde olumlu bir etkisi olduğunu göstermiştir.

Anahtar Kelimeler: Çekirdeklenme kinetiği, iki-fazlı mikroakışkan sistem, aşırı doygun çözelti, kristalleşme, pikoreaktör,.

ACKNOWLEDGMENTS

I would like to appreciate my supervisor, Dr. Selis Önel for accepting me into her lab and for creating a friendly environment for student-supervisor relationships – this is not found everywhere. Thank you for the corrections, motivations, and criticisms as well.

My heartfelt appreciations also go to the Presidency for Turks Abroad and Related Communities (YTB) for giving me this unique opportunity to study in Turkey. Teşekkürler Türkiye!!!

I would like to acknowledge TÜBİTAK, The Scientific and Technological Research Institution of Turkey, for providing the funds for this research through a 1001 project (220M002).

I would like to extend my thanks to Dr. Burcu Akata Kurç and her lab for providing the recipes for the UiO-66 precursor solutions.

They say good friends are like four-leaf clovers; hard to find and lucky to have. Such is an understatement when describing my lab mates. On this note, I would like to extend my appreciation to Buse, Anıl, Gaye and Gökçen for not only making my stay in the lab comfortable but for adding sweet flavors to my overall experience in Turkey. İyi ki varsınız.

To everyone who has contributed in one way or the other to the success of my master's degree program I say thank you.

On a final note, my heartfelt appreciation goes to my backbone, the model of what motherhood should be. Love you, mum!

Tijani Ahmed AHMED

August, 2022

TABLE OF CONTENTS

ABSTRACT i

ACKNOWLEDGMENTS viii

TABLE OF CONTENTS ix

LIST OF FIGURES xii

LIST OF TABLES xv

SYMBOLS AND ABBREVIATIONS xvi

1. INTRODUCTION 1

1.1 Background to the study 1

1.2 Aim and Objectives 4

2. GENERAL INFORMATION 5

2.1 Two-Phase Microfluidic Systems 5

2.2 Controlling Nucleation And Growth Of Crystals In A Microfluidic System 6

2.3 Nucleation and Growth Model 10

2.4 Nucleation Kinetic Modeling In Microfluidic Systems 11

2.5 Metal-Organic Frameworks (MOFs) 12

2.5.1 Structure of Metal-Organic Frameworks (MOF) 12

2.6 Microfluidic Systems for Crystallizing MOF Precursor Solutions 15

2.7 Other Methods of Crystallizing MOF Precursor Solutions 18

2.7.1 Batch Solvo (hydro)thermal Synthesis 19

2.7.2 Microwave-Assisted synthesis 22

2.7.3 Sonochemical Synthesis 23

2.7.4 Electrochemical Synthesis 24

2.7.5 Mechanochemical Synthesis 25

3. MATERIALS AND METHODS 26

3.1 Materials 26

3.1.1 Microfluidic Device 26

3.1.2 Fabrication of Microfluidic Device 28
3.1.3 Preparation of Solutions 29
3.2 Experimental Methods 30
3.2.1 Experimental Setup 30
3.2.2 Optimization Of Droplet Generation 31
3.2.3 Crystallization Experiment 34
3.2.4 Kinetic Model Calculations 36
4. RESULTS AND DISCUSSION 38
4.1 Optimization of Droplet Generation in the Cold Region 38
4.1.1 Optimization of Droplet Generation in the Cold Region 38
4.1.2 Optimization of Droplet Generation in the Hot Region 41
4.2 Crystallization of the Precursor Solution 42
4.2.1 Effect of Droplet Size on Crystallization of time of the Precursor Solution. 43
4.2.2 Effect of Temperature on Crystallization of UiO-66 Precursor Solution 44
4.3 Kinetic Model Calculation 46
4.4 Investigation of Droplet Shrinkage in Silicone Oil 50
5. CONCLUSIONS 52
6. REFERENCES 54
APPENDIX 59
Appendix 1 – Detailed Calculation of Kinetic parameters 59
Appendix 2- Microfluidic Two-Phase Flow Optimization Results 61
Appendix 3– Table of Values for calculating the residence time at 70 µm and 80 °C 62
Appendix 4 – Table of Values for calculating the residence time at 90 µm and 80 °C 63
Appendix 5 - Table of Values for calculating the residence time at 110 µm and 80 °C 64
Appendix 6 - Table of Values for calculating the residence time at 70 µm and 50 °C 65
Appendix 7- Table of Values for calculating the residence time at 70 µm and 80 °C 66
Appendix 8 - Table of Values for calculating the residence time at 70 µm and 100 °C 67

Appendix 9 – SEM Image for crystallization at 80 ºC and 70 µm Droplet Size 68
Appendix 10- Table Showing the Change in area, volume, and concentration at 50 ºC and 70 µm droplet size 69
Appendix 11- Table Showing the Change in area, volume, and concentration at 80 ºC and 70 µm droplet size 70
Appendix 12- Table Showing the Change in area, volume and concentration at 100 ºC and 70 µm droplet size 71
Appendix 13 – Originality Report 72
Currıculum vıtae 73

LIST OF FIGURES

Figure 2.1. The extent of crystallization α(t) plotted against time t (closed symbols) and the corresponding Gualtieri fitting (solid curves) 8

Figure 2.2. The extent of crystallization α(t) plotted vs time (closed symbols), the corresponding Gualtieri fitting (red curve), and probability of nucleation 8

Figure 2.3 Optical and SEM images of the (A) non-hydrated HKUST-1 crystals formed from precursor solutions dissolved in ethanol and (B) hydrated HKUST-1 crystals formed from precursor solutions..... 9

Fig. 2.4 SEM images from HKUST-1 crystals synthesized dissolved in an ethanol-water mixture (50:50)..... 10

Figure 2.5 La Mer Model for Describing Nucleation and Growth 11

Figure 2.7. Some Examples of Linkers used in the synthesis of MOF crystals..... 14

Figure 2.8. Different MOF structures with the terephthalate (BDC) dianion as a linker..... 14

Figure 2.9. Microfluidic Setup for MOF synthesis 15

Figure 2.10. Conventional solvothermal Crystallization. 19

Figure 2.11 Structures of CAU-10 (top left), Ce-UiO-66 (bottom left), as well as narrow- (top right) and open-pore form (bottom right) of standard Al-MIL-53 with unit cell edges. 20

Figure 2.12. Microwave-assisted solvothermal synthesis of MOF structures. 23

Figure 2.13 Sonochemical synthesis of MOF structures..... 23

Figure 2.14. Electrochemical syntheses of MOF Crystallization 24

Figure 2.15. Mechano-chemical synthesis of MOF crystallization 25

Figure 3. 1 PDMS Microfluidic Device 27

Figure 3. 2 Microfluidic device mounted on 3D printed holder with thermocouples and the heater. 27

Figure 3. 3. Vacuum Plasma activation setup for microfluidic device fabrication..... 29

Figure 3. 4 Complete Experimental Setup. 31

Figure 3. 5. General view of the microfluidic device used in the studies, inlet ports, and a zoomed-in view of the droplet formation region 32

Figure 3. 6 Examples of Droplet measurements at different sections of the device..... 33

Figure 3. 7. Droplet measurements being taken at the serpentine section 34

Figure 3. 8. Crystals stick to the wall of the channels during crystallization. 36

Figure 4. 1. Relationship between Droplet Sizes and flow rate ratio (Qd/Qc) 39

Figure 4. 2 Relationship between the average interdroplet distances and flow rate ratio (Qd/Qc) 40

Figure 4. 3. Relationship between flow rate ratio versus % shrinkage from the droplet formation region to the heating region 41

Figure 4. 4. Relationship between droplet sizes and serpentine number as they travel along the serpentine until nucleations were observed. 42

Figure 4. 5. Relationship between the residence time and droplet size for nucleation of UiO-66 precursor solution. 43

Figure 4. 6. Schematic diagram showing the serpentine where nucleations of UiO-66 precursor solution were first observed and the effect of droplet size on nucleation time → Make yellow circle smaller and red circle larger and correct their place on the serpentine!!! Orange and red will change place!!! 44

Figure 4. 7. Effect of temperature on nucleation time of UiO-66 precursor solution 45

Figure 4. 8. Schematic representation of points of nucleation of UiO-66 precursor solution at different temperatures with their final diameters just before nucleations were observed. 45

Figure 4.9 Rate of nucleation as a function of temperature and supersaturation ratio ... 47

Figure 4.10 Plot of Nucleation kinetic rate constant versus the inverse of temperature 48

Figure 4. 11. XRD pattern obtained from crystallization of UiO-66 precursor solution at 50 and 80 ^{o}C. 49

Figure 4.12. Effect of temperature on the crystallinity of UiO-66 MOF crystals found in the literature. 49

Figure 4.13: Shrinking behavior of the droplet formed by the precursor solution in the silicone oil. 50

Figure 4.14. Shrinkage behavior of the droplet formed by the BDC+DMF solution in the silicone oil 50

Figure 4.15: Shrinkage behavior of droplet formed by $ZrCl_4$+DMF solution in silicone oil..... 51

Figure 4.16. Shrinkage behavior of droplets formed by pure DMF in silicone oil 51

LIST OF TABLES

Table 2.1 Summary of MOF crystallization from solutions in microfluidic reactor systems 18

Table 4.1 Nucleation Parameters 46

Table 4.2 Arrhenius Calculation Parameters 48

SYMBOLS AND ABBREVIATIONS

Symbols

J	Rate of droplet nucleation (s^{-1})
Qd	Flow rate of the dispersed phase (μL/min)
Qc	Flow rate of the continuous phase (μL/min)
N	Number of nucleated droplets
k_N	Nucleation kinetic rate constant (s^{-1})
S	Supersaturation ratio (dimensionless)
k_o	Arrhenius constant ($J.mol^{-1}.K^{-1}$)
D_i	Initial diameter (μm)
D_f	Final Diameter (μm)
t	Time (s)
T	Temperature (K)
E_N	Activation energy for nucleation ($KJmol^{-1}$)
D_h	Hydraulic diameter of the microfluidic device (μm)
D*	Droplet diameter divided by the hydraulic diameter (dimensionless)
V_m	Molecular volume of the crystallizing substance
K	Boltzmann's constant (JK^{-1})
R	Universal gas constant ($J.mol^{-1}.K^{-1}$)
γ	Interfacial tension (Nm^{-1})

Abbreviations

PDMS	Polydimethylsiloxane
ITO	Indium-tin-oxide (ITO)

BDC	1,4-benzenedicarboxylic acid
$ZrCl_4$	Zirconium (IV) chloride
DMF	N,N-dimethylformamide
MOF	Metal-organic framework
SEM	Scanning electron microscope
XRD	X-ray diffraction
UiO	University of Oslo

1. INTRODUCTION

1.1 Background to the study

The effects of thermodynamic conditions on the kinetics of nucleation from supersaturated solutions have been of great interest in controlling the synthesis of nano/micro-particles with advanced physical, chemical, and optical properties. Microfluidic systems are turbulence-free, highly miniaturized devices with networks of microchannels through which fluids flow or in which they are contained. Microfluidic devices have dimensions and unique geometries suitable for very small reagent volume use, thorough and rapid fluid mixing, efficient heat and mass transport, faster synthesis duration, ease, and the possibility of automated control [1-5]. These advantages associated with microfluidic devices have made them useful in biology and biotechnology, chemistry, material sciences, and biomedical engineering. In biology and biotechnology for example microfluidic devices are employed in protein crystallography and synthesis of pharmaceutical products [6]. In chemistry and material sciences and engineering, microfluidic systems are increasingly becoming popular in the crystallization of various micro and nanomaterials from solutions and carrying out so many chemical syntheses [7, 8]. When used as synthesis vessels they are referred to as microreactors [9, 10]. One of the prominent areas in which microfluidic devices have been found useful is in the bottom-up crystallization study, especially from supersaturated solutions. More recently, microfluidic systems have been employed in the crystallization of metal-organic frameworks (MOF) precursor solutions, a more complex solution.

Crystallization of metal-organic frameworks (MOFs) precursor solutions, have attracted widespread interest and have become one of the fastest-growing fields, due to their great potential in industrial applications [11]. This is evident from the growing number of works and publications emanating from various disciplines, such as chemical engineering, chemistry, and materials science and engineering. MOFs are a porous coordination network of materials formed as a result of the bonding between different organic ligands and metal-based nodes. MOFs consist of two major components - a metal ion and organic linkers or bridging ligands [12]. This class of crystalline materials, in which metal nodes are surrounded by organic linkers, are joined together by coordination

bonds. The structure of MOF can be likened to a sponge, which accounts for its high porosity and high surface area. Owing to their porosity [13, 14], tremendously large surface areas [15, 16], and adjustable pore characteristics [16, 17], these solids show great promise for a wide range of industrial applications.

The ability to crystallize MOF precursor solutions at relatively low pressure and temperature [18], coupled with the high surface areas has attracted serious interest in recent years. These properties are exceptionally useful in operations, such as drug delivery, gas storage, catalysis, ion exchange, separation, wastewater treatment, and as membrane materials [14, 18, 19]. The challenges with studying crystallization from supersaturated precursor solutions encompass the deliberate control of the structure, and therefore the properties and functions of the desired crystals, as many synthetic factors play subtle roles in the crystallization process. Among many influencing factors, the nature of solvents, molar ratio of reactants, mixing, pH, and temperature are crucial parameters that determine the overall efficiency of the crystallization process [20-25].

Various methods of carrying out crystallization from supersaturated MOF precursor solutions include the conventional batch solvothermal process, sonochemical, microwave, electrochemical, aerosol, mechanochemical, flow chemistry, and microfluidic synthesis structures [26, 27].

In crystallizing from MOF precursor solutions (bottom-top synthesis), influences of parameters, such as solvent selection [28, 29], pH [13, 30], and temperature [31] have been investigated. Achieving real-world applications lies in synthesizing MOFs crystal in commercial quantity while juxtaposing quality with cost of production. Despite the advances made so far in the crystallization processes of supersaturated solutions, there seem to be few commercially available MOF crystal products. This suggests that an effective and efficient nucleation technique that would ensure continuous production, high yield, and quality remains a critical bottleneck for realizing efficient and effective crystallization from supersaturated precursor solutions at a large scale for practical applications.

Due to the various shortcomings associated with the conventional batch method of crystallization, such as long synthesis time, poor mixing, and poor heat distribution, researchers have shifted their focus to continuous mode, using microfluidic systems since

Faustin et. al [32] first crystallized HKUST-1, MOF-5, IRMOF-3, and UiO-66 successfully in a continuous microfluidic system.

Microdroplets offer attractive means of studying nucleation and crystal growth processes using microfluidic devices [33]. Miniaturization of the reaction environment and the power of observation and control over the system make microfluidic devices effective tools to understand the phenomena related to phase transitions in supersaturated solutions and optimizing the precursor solution to generate monodispersed droplets and interdroplet distances for effective nucleation behavior.

Better mixing, lower energy, and chemical consumptions, as well as better controllability and highly scalable characteristics of the microfluidic channels, offer a better alternative to carry out crystallization from supersaturated solutions. Furthermore, microfluidic systems offer a high degree of operational flexibility such as automated control, integration, and the potential of live quality monitoring through a transparent system or computer programming. Thus, this approach is unique and highly advantageous over the batch method for carrying out crystallization from solutions.

In the various fields where crystallization is needed, chemical engineers need to develop a robust crystallization process that delivers high-quality crystals with high yield and suitable properties conducive to suitable real-world applications (e.g., purity, polymorphism, and particle size distribution). To achieve this, certain basic data on nucleation kinetics, crystal growth, and phase transitions must be accurately determined. Since nucleation is inherently a stochastic phenomenon [34], it is extremely difficult to reproduce, and even very carefully conducted experiments can have substantial variability [35, 36].

In this study, a transparent thermo-fluidic device on an inverted microscope was used to observe the solidification kinetics in monodisperse micro-droplets of a supersaturated solution. The device has a flow-focusing design for uniform droplet generation and a serpentine section integrated with a transparent ITO heater, micro-thermocouples, and a power supply with a PID temperature controller. This process involved optimization of two-phase flow parameters to obtain the desired droplet sizes and flowrates for effective crystallization study of a UiO-66 (UiO stand for University of Oslo) MOF precursor solution obtained from Dr. Burcu Akata Kurç's laboratory at Middle East Technial

University (METU) in a two-phase flow microfluidic system, and the effects of temperature and droplet sizes on the nucleation kinetics were investigated.

1.2 Aim and Objectives

The main aim of this work is to optimize the two-phase flow conditions in a flow-focusing microfluidic device to obtain the desired droplet sizes by varying flow rates of the solution and to investigate the kinetics of nucleation from a supersaturated solution.

The specific objectives involve:

- Optimizing the two-phase parameters by generating picolitre droplets by varying the flow rate of the dispersed and continuous phases.
- Plotting the droplet sizes and interdroplet distances at various flow rates against the flow rates.
- Studying the crystallization process of a UiO-66 precursor solution prepared in Prof. Dr. Burcu Akata Kurç's laboratory at Middle East Technical University, taking into consideration the effect of temperature and size of the droplet serving as picoreactor.
- Extraction of the kinetic data from the nucleation of the supersaturated solution using the classical nucleation model.
- Characterization of the particles formed in the droplets using a scanning electron microscope (SEM) and X-ray diffraction (XRD).

2. GENERAL INFORMATION

2.1 Two-Phase Microfluidic Systems

Two-phase microfluidics, as the name implies, involve the introduction and manipulation of two immiscible fluids at the micro and nanoscale. Two factors that must be considered when studying two-phase micro and nanofluidics are: 1. the nature of the immiscible fluids, which may have different chemical compositions (liquid/liquid) or different physical states (gaseous/liquid) and 2. the properties of the devices to be scaled down to the micro or nanoscale [37].

There has been a recent surge of interest in microfluidic systems for manipulating two-phase fluids. This is because most studies of chemical and interfacial phenomena and their applications rely on two-phase flow. After all, fluids of interest in nature, chemical sciences, and engineering are rarely in a single phase [38]. When two phases are injected into a microfluidic device one (the continuous phase) often preferentially wets the channel and encapsulates or cuts the other (dispersed phase) into discrete droplets [39]. At this miniaturized scale, the influence of gravity becomes less important [40]. Dynamical responses of fluids in two-phase microchannels are often successfully characterized by some dimensionless numbers, such as the Reynolds number (Re) and capillary number (Ca) [41].

The movement of the fluids in two-phase microchannels is driven by internal forces as a function of the nature of the fluid and channel properties or by external forces such as electrical, magnetic, thermal, and photonic forces [37]. Fluid flow in a cross-sectional channel follows the Poiseuille's law as shown below:

$$\boldsymbol{Q} = \int \boldsymbol{v}_{\boldsymbol{i}} \boldsymbol{dA} \approx \frac{\Delta \mathbf{P}}{\boldsymbol{R}} \qquad 2.1$$

where $\boldsymbol{Q}$ (m^3/s) is the volumetric flow rate, $\boldsymbol{v}_{\boldsymbol{i}}$ is the flow velocity (m/s) at position i (v_i is constant in flat flow and $\approx 0.5 v_{max}$ in parabolic flow), A (m^2) is the cross-sectional area, ΔP (Pa) is the pressure difference between the two ends of the channel, R_{hy} ($kgs^{-1}m^{-4}$) is the hydrodynamic resistance, which approximately is given by:

$$Rhy \approx \eta L C^2 A^{-3} \qquad 2.2$$

2.2 Controlling Nucleation And Growth Of Crystals In A Microfluidic System

In recent times, the subject of crystallization has received enormous attention owing to its vast industrial and scientific applications. Crystallization from a supersaturated solution is the most widely used crystallization method in the pharmaceutical industry [42] and recently in the crystallization of MOF structures from supersaturated precursor solutions. Nucleation refers to the first stage that occurs in the crystallization process of a solution, a liquid, or a vapor. And growth involves ions, atoms, or molecules arranging in a pattern characteristic of a crystalline solid and thereby, forming a site upon which additional particles are deposited. However, obtaining the desired crystal quality lies in the ability to overcome the difficulties in monitoring and controlling the nucleation and growth processes [43]. In crystallizing precursor solutions great attention must be paid to controlling the processes, as they are very sensitive to even the smallest changes in the nucleation conditions.

Microfluidics system, especially two-phase flow conditions used in this study is a relatively new, but promising method of studying nucleation and crystal growth experiments. Its high-level diffusion control, concentration, flow dynamics, water-oil interface, liquid-gas interface [44], excellent mixing, and low reagent consumption [45] are few of the reasons for the great attention it has been receiving recently. Microfluidic systems have been used to study protein crystallization [43, 46], pharmaceutical products as well as MOFs [45]. Controlling nucleation and crystal growth is so important because the crystallization process requires a precise balance between crystal formation and dissolution to allow for sufficient reorganization and defect reparation during the early stages of crystal growth. The miniaturization of the microfluidic reaction system leads to short diffusion lengths, ensures rapid and thorough mixing of reagents, fast heat and mass transport, as well as precise control of residence times (order of milliseconds). These are all critical to controlling the nucleation and growth of crystals [45]. Hence, controlling the flow rate, solvent selection, residence time, and concentration of the precursor or pH can determine the rate of nucleation and growth of crystals, as well as the shapes and morphologies. In this study, precise control of flow rates of the continuous phase (silicon oil) and dispersed phase (UiO-66 MOF precursor solution) is adopted to control the droplet (microreactor) size.

Bagi et. al [45] carried out a solvothermal crystallization study to determine the kinetics and control of crystal size of MOF-808 in a continuous microfluidic flow reactor. They took the advantage of the fact that residence time can be precisely controlled in a biphasic liquid−liquid continuous flow operating reactor, and thus kinetic data can be extracted from the system. In their experiment, silicone oil was used as the continuous phase because it preferentially wet the PTFE tubing and encapsulates the slugs (μL droplets) of the dispersed phase containing the MOF precursors. The synthesized MOF crystals were collected, filtered, and washed with N,Ndimethylformamide (DMF), and acetone, and then characterized with powder X-ray diffraction (PXRD). The formation of crystallinity was measured using the extent of crystallization ($\alpha(t)$) as a function of time (equation 2.3).

$$\alpha(t) = \frac{I(t)}{I_{max}} \qquad (2.3)$$

Since the crystallization behavior strongly depends on reaction conditions, the influence of temperature (110, 120, 130, and 150 °C) and linker concentration (1×, 2×, 2.5×, and 3×) in the reaction mixture were studied and the curves are shown in Figure 2.1 a and b respectively. Gualtieri model (equation 2.4) was used to evaluate the kinetics of the crystallization curves by fitting the data (closed symbols) in Figure 2.1. The values for both k_G and k_N were found to increase with temperature but for each temperature $k_N < k_G$ suggesting that the nucleation is slower than crystal growth. Since the nucleation sites are not directly visible, they are modeled by defining the probability of nucleation P_N (equation 2.5). It was found that as temperature increases faster nucleation rate is achieved. Figure 2.2 shows the plot of P_N versus t (blue curve) for the crystallization curve obtained at 130 °C and 3×linker concentration. Activation energies $E_A(N)$ and $E_A(G)$ for nucleation and growth, respectively were calculated using the Arrhenius equation (equations 2.6 and 2.7). Activation energies for nucleation $E_A(N)$ and growth $E_A(G)$ determined from Arrhenius plots were 64.7 ± 4 and 59.2 ± 5kJ·mol^{-1}. In this work, the flow rate was used for tuning MOF crystal size with narrow distribution. An increase in flow rate was found to increase the crystal size. For a constant residence time increasing the flow rate flow-mediated transport of precursor solution to the nucleation site leads to faster growth with a decrease in nucleation rate due to faster consumption of the reagents. This phenomenon is in line with La Mer's model as described by Shield et. al in their study of the Coarsening Kinetics of Thiolate-Capped Gold Nanocrystals [47].

$$(\alpha) = \frac{1}{1+e^{-(t-a)/b}}\left[1-e^{-(k_G.t)^n}\right] \quad (2.4)$$

$$P_N = \frac{dN}{dt} = e^{-((t-a)^2/2b^2)} \quad (2.5)$$

$$k_N = Ae^{-\left(\frac{E_a(N)}{RT}\right)} \rightarrow \ln k_N = \ln A - \frac{E_a(N)}{RT} \quad (2.6)$$

$$k_G = Ae^{-\left(\frac{E_a(G)}{RT}\right)} \rightarrow \ln k_G = \ln A - \frac{E_a(G)}{RT} \quad (2.7)$$

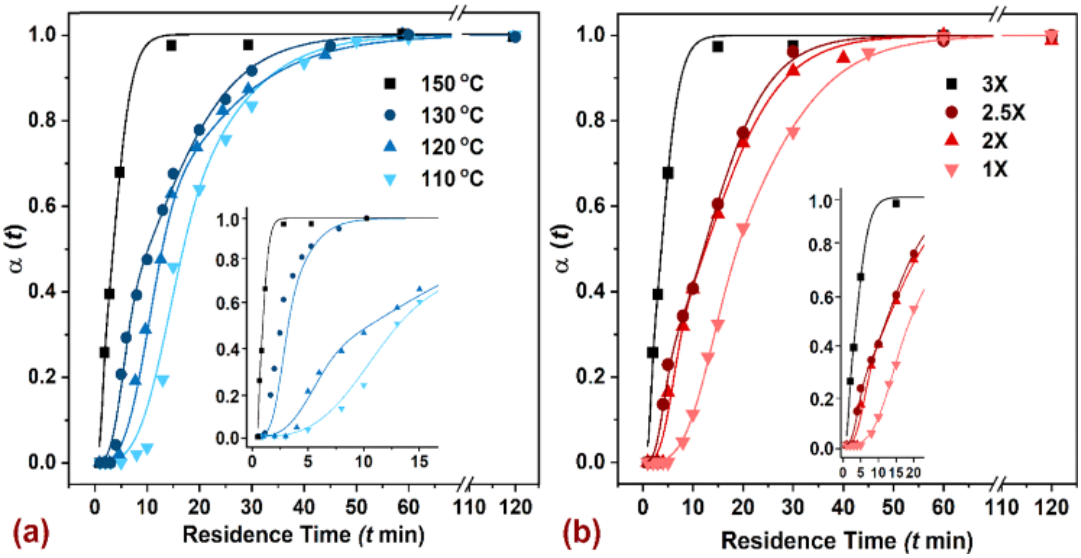

Figure 2.1. The extent of crystallization α(t) plotted against time t (closed symbols) and the corresponding Gualtieri fitting (solid curves) [45]

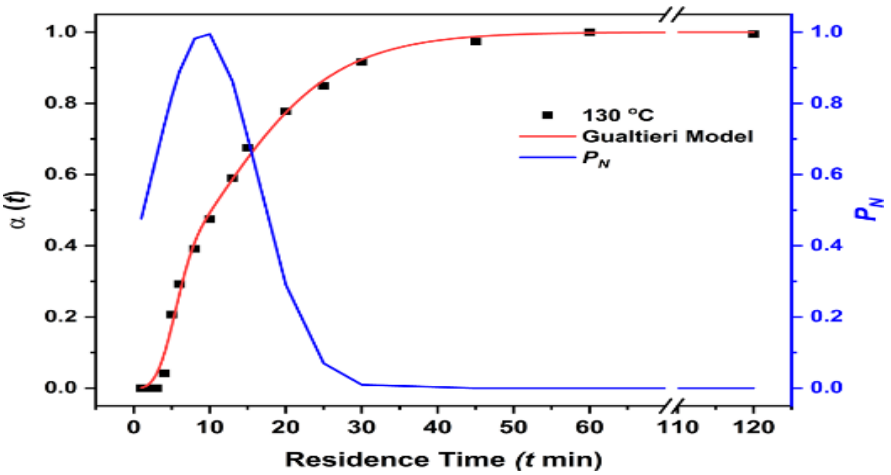

Figure 2.2. The extent of crystallization α(t) plotted vs time (closed symbols), the corresponding Gualtieri fitting (red curve), and probability of nucleation [45]

Solvent selection and pH effects of the precursor can be used to control the crystallization during MOF precursor solutions. Acidic and basic pH can lead to reduced crystal size and reduced size distribution. Coliaie P., et. al [46] studied the effect of solvent selection and

pH in a patterned microfluidic mixer device on HKUST-1 MOF. The shape of crystals resulting from crystallizing MOF particles from solution was found to be a function of the solvent and pH used according to Coliaie P., et. al. Solvent was observed to affect the coordination of the Cu atoms and changes in the direction of the crystal growth. When ethanol was used to dissolve the organic linker, HKUST-1 crystals were formed (Figure 2.3a), but when the solvent was changed to ethanol-water mixture hydrated crystals with an elongated rod-shaped morphology were observed (Figure 2.3b). To study the effect of pH, acetic acid and pyridine were used as acidic and basic modulators. While the synthesized crystals in the presence of acid modulators had a round-shape morphology (Figure 2.4a), those synthesized without modulators and with basic modulators had octahedral morphology (Figure 2.4 b & c). Hence, dimensionality was enhanced by adding basic modulators. Both acid and basic modulators were also found to decrease crystal size and narrow size distribution (figure 2.4d).

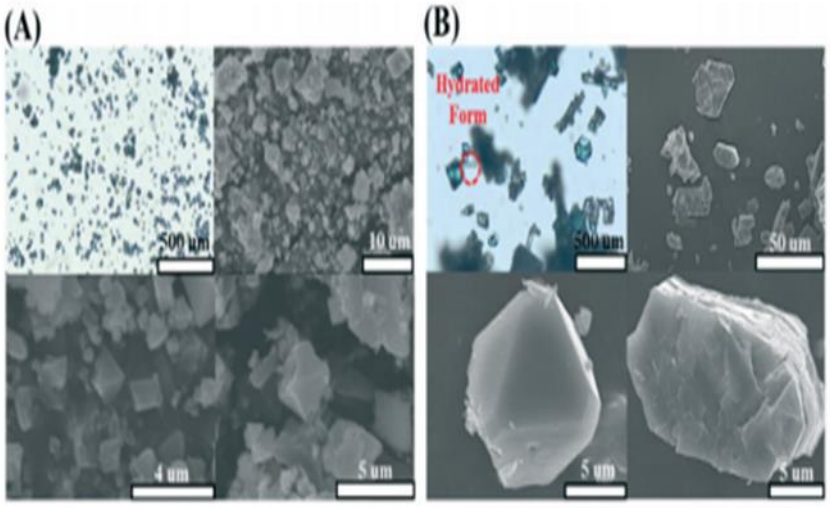

Figure 2.3 Optical and SEM images of the (A) non-hydrated HKUST-1 crystals formed from precursor solutions dissolved in ethanol and (B) hydrated HKUST-1 crystals formed from precursor solutions [46]

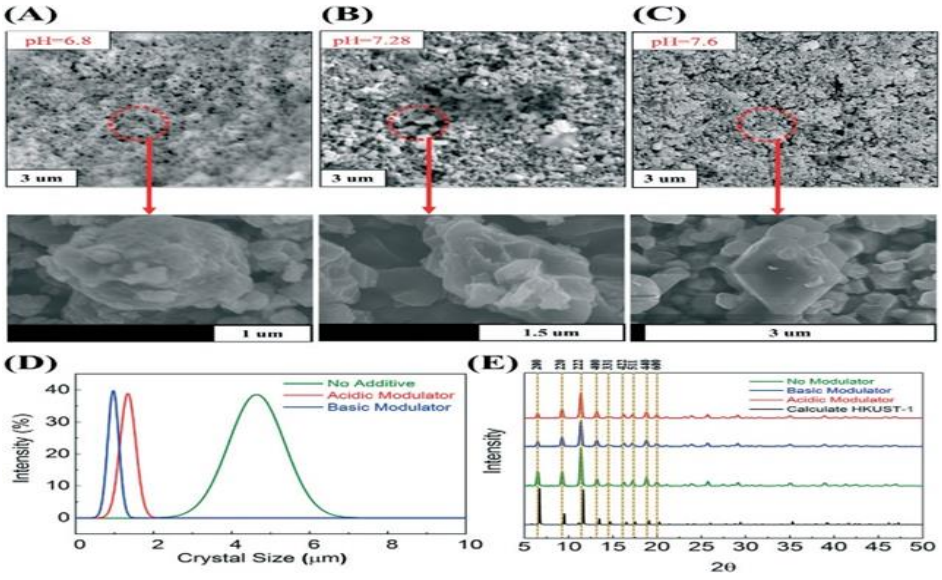

Fig. 2.4 SEM images from HKUST-1 crystals synthesized dissolved in an ethanol-water mixture (50:50) [46] .

2.3 Nucleation and Growth Model

Many synthetic factors are considered when synthesizing nanoparticles. The ideal goal is to get nanoparticles with controlled size and narrow size distribution. The La Mer model (Figure 2.5) for monodisperse colloid growth, developed in the 1950s for colloidal sulfur, provides a simple conceptual explanation for the nucleation and growth of nanoparticles. When a reaction is mixed or otherwise initiated, precursors accumulate (stage I), resulting in some degree of supersaturation. When the degree of supersaturation exceeds the critical threshold for nucleation, instantaneous nucleation (II) occurs in order of a few seconds, reducing the degree of supersaturation. When the rate of nucleation exceeds the rate of precursor formation, the precursor concentration drops back below the nucleation threshold.

Nanoparticle growth can then proceed via a variety of pathways such as Monomer addition in which additional precursor units from solution attach to the preformed nuclei or Ostwald ripening in which energetically unfavorable small nuclei redissolve and attach to thermodynamically more favored larger nuclei or coalescence in which multiple nanoparticles come together and fuse (III). This framework allows us to consider methods to control both size and size distribution [48, 49].

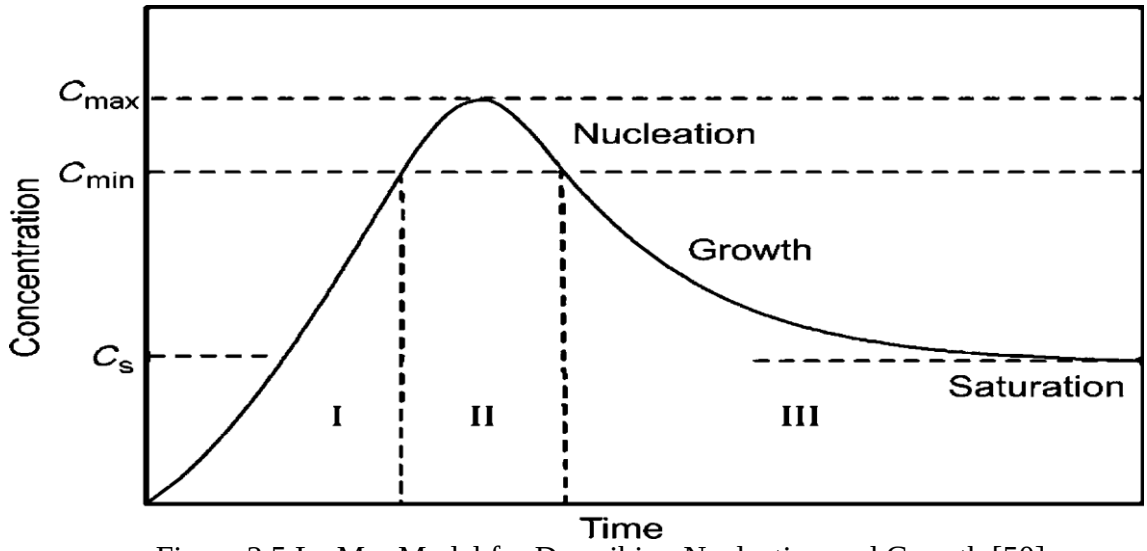

Figure 2.5 La Mer Model for Describing Nucleation and Growth [50]

2.4 Nucleation Kinetic Modeling In Microfluidic Systems

One of the most important advantages of microfluidic devices for crystallization is their usefulness for generating kinetic data because they offer good control and improved transport of heat and mass, low gravitational effect, and few impurities. In addition, two-phase flows can generate nearly monodisperse droplets in hundreds of carefully designed channel geometries, which present a large set of independent nucleation events for performing statistical analysis [42]. The classical nucleation theory (CNT) has been the most widely used model to determine the kinetic parameters of crystallization carried out in microfluidic systems from supersaturated solutions [42, 45, 51-58]. A nucleation is purely a stochastic event and the CNT describes the probability of finding nucleation by equation 2.8

$$P_0 = \frac{N_0}{N_t} \quad (2.8)$$

Where P_0 is the probability of finding no crystal in a droplet, N_0 and N_t are the numbers of empty droplets and the total number of droplets under consideration.

The probability that one or more crystals occur is given by

$$1 - P_0 \quad (2.9)$$

The probability of finding no crystal at time t when related to the rate of nucleation *J* (equation 2.10)

$lnP_0 = -JVt$ (2.10)

However, the plot of lnP_0 vs t hardly gives a straight curve suggesting heterogeneous nucleation caused by the presence of active centers or impurities.

Despite the complicated nature of crystallization in drops due to nucleation, crystallization growth rate dispersion, and Oswald ripening all taking place, a simple model that describes crystallization from a supersaturated solution is the classical nucleation theory [52, 56]

$$J = A \exp\left(\frac{-16\pi\gamma^3 V_m^2}{3(KT)^3(lnS)^2}\right) = Aexp(\frac{\Delta G^*}{KT}) \qquad (2.11).$$

Where J is the rate of nucleation (s^{-1}) γ is the interfacial tension between the crystal and solution (N/m), V_m is the molecular volume of the crystallizing molecule (m^3/mol), k is Boltzmann's constant (1.38 x 10^{-23} JK^{-1}) and T is the absolute temperature (K). S is the relative supersaturation ratio and ΔG^* is the critical Gibb's free energy.

2.5 Metal-Organic Frameworks (MOFs)

Metal-organic frameworks (MOFs) are porous hybrid crystalline materials having metal-based nodes connected by organic ligands [59, 60]. Some of the prominent characteristics of MOFs are high turnability, porosity, and large surface areas. In addition to gas storage, catalysis, ion exchange, and separation, MOFs are also potential candidates for small-scale robotic platforms for applications in environmental remediation, targeted drug delivery, or nanosurgery [60-63]. In addition to direct use, MOFs have also been employed as carrier substrates for nanomaterials or as sacrificial templates/precursors for the fabrication of various functional nanostructures [61].

2.5.1 Structure of Metal-Organic Frameworks (MOF)

The metal-organic framework (MOF) structure comprises two building units – the primary building units (PBUs) shown in figure 1, and the secondary building units (SBUs).

2.5.1.1 Primary Building Units (PBUs)

The PBUs consist of metal nodes and organic ligands. The metal nodes can be atoms, ions, or clusters. The metal ions are usually from elements found on the first row of the transition series in the periodic table, such as Cr^{3+}, Fe^{3+}, Co^{2+}, Zn^{2+}. Some alkali metal ions, such as Li^{+1}, Na^{+1}, K^{+1} ions, alkaline-earth metal ions, such as Be^{+2}, Mg^{+2}, Ca^{+2}, and rare earth metal ions, such as Sc^{+3}, Y^{+3}, La^{+3}, are also used to form the metal nodes that connect the organic linkers [12].

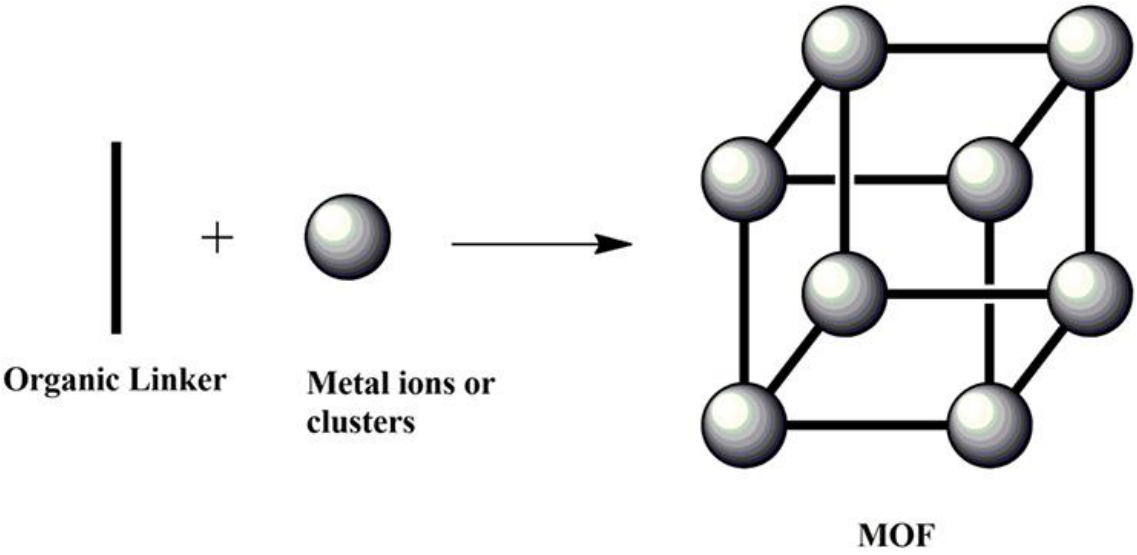

Figure 2.6. A simplified MOF structure showing the primary building units (PBUs) [64].

The organic linkers, some of which are shown in Figure 2.7, which usually contain functional groups, such as carboxylate, phosphate, sulfonate, amine, and nitrile, connect the metal nodes by coordination bonds to give periodic porous structures. The structure and properties of MOF crystals are regulated by the coordination mode and the geometric configuration of the metal cluster and organic ligand. So, different combinations of these structural elements lead to an enormous number of MOFs [65].

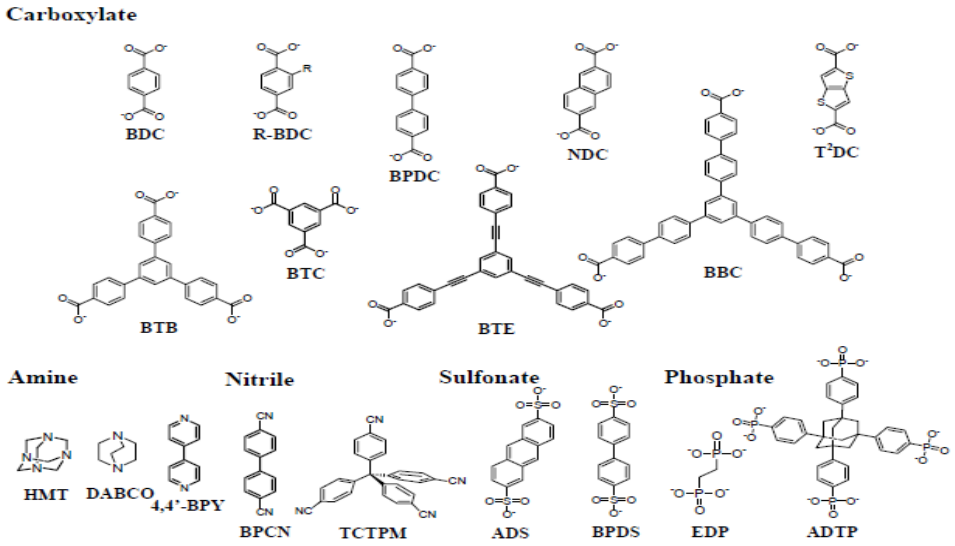

Figure 2.7. Some Examples of Linkers used in the synthesis of MOF crystals [12]

2.5.1.2 Secondary Building Units (SBU)

Generally, organic linkers are not bonded to a metal ion alone. They are connected to a metal-oxygen-carbon cluster. This cluster is known as the secondary building unit (SBU). MOF topology depends largely on the SBUs because the network connectivity of the building units is a major determinant of the properties of a MOF structure. Hence, building monomers and their orientations are carefully selected and controlled to reflect the needs. Figure 2.8 shows the different MOF structures that can be formed with the terephthalate (BDC) dianion as the secondary building units.

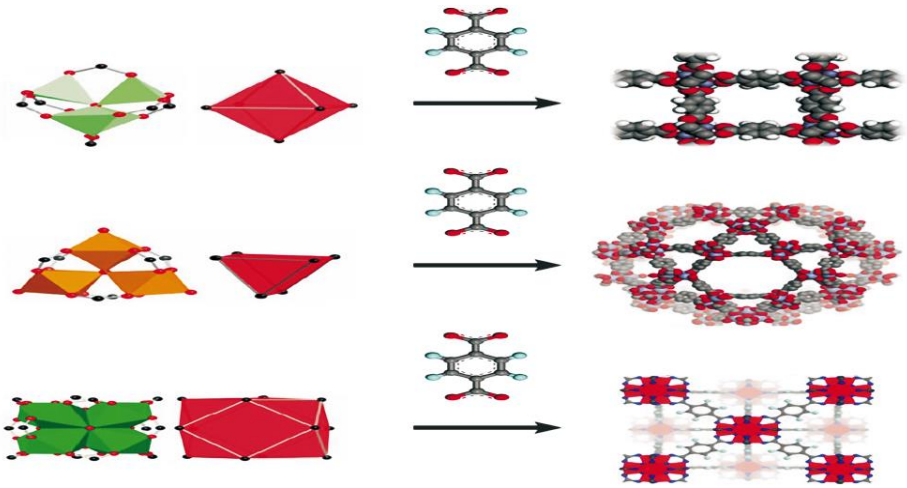

Figure 2.8. Different MOF structures with the terephthalate (BDC) dianion as a linker [26].

2.6 Microfluidic Systems for Crystallizing MOF Precursor Solutions

The problems of impurities and inhomogeneity in solution mixtures are often faced in the traditional methods of crystallization. Microdroplets offer attractive means of studying crystallization processes using microfluidic devices [33]. There is a high interest in searching for suitable, economically viable, and efficient methods of carrying out crystallization of pharmaceutical products and recently, MOFs. Researchers have been beaming their searchlights on the best methodologies to adopt in crystallizing MOF crystals with the prospect of higher yield, lower cost, and environmentally benign operations. Employing microfluidic devices serve as a viable solution to these problems [66]. Microchannels provide a better mixing environment for the precursor solutions and solvents. Two-phase flow with microdroplets ensures that small quantities of reagents are used with multiple droplet formations to generate a large amount of data for statistical analyses [33]. Fig. 2.9 shows an example of a microfluidic setup for MOF synthesis.

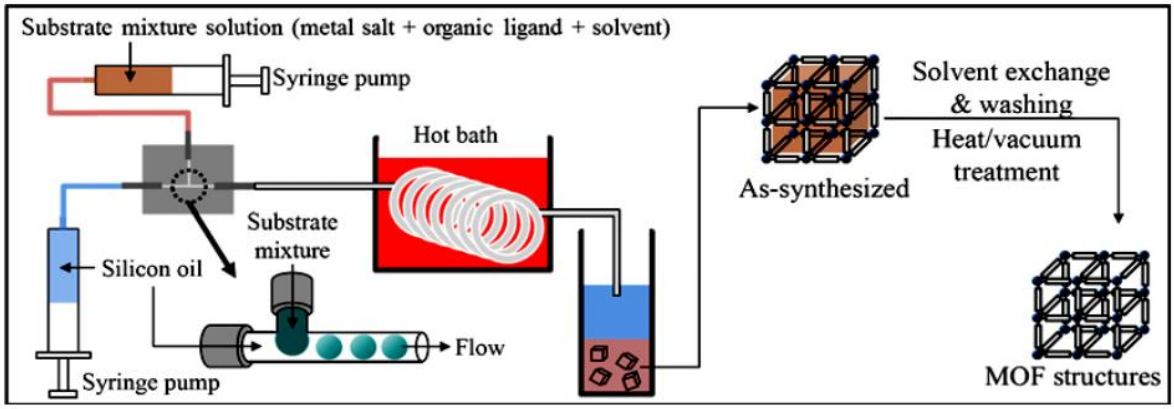

Figure 2.9. Microfluidic Setup for MOF synthesis [66]

Cacho-Bailo et al. [18] used a microfluidic method to synthesize ZIF-7 and ZIF-8 continuous membranes on the inner surface of a 520 μm (outer diameter, OD) polymeric (polysulfone) hollow fiber (HF). Suitable solvents, i.e. methanol for ZIF-8 and ethanol for ZIF-7, were used to wet the polymeric HF for 75 min at 100 μL/min. The reagent streams were then pumped through the HF with a total flow rate of 100 μL/min. The pure solvent was pumped again for 75 min using the same flow rate after the crystallization of the membrane had been completed. This is to wash the inner surface, to ensure laminar flow with 9.4 seconds of residence time within the HF. MOF crystals were collected,

washed, and dried. It was observed from the SEM images of the synthesized MOF crystals were successfully intergrown giving rise to a thin, continuous, and dense ZIF-7 layer of (2.4 μm) and ZIF-8 (3.6 μm) with good adherence. XRD and FTIR analyses showed that in the case of ZIF-8, the membrane XRD pattern matched that of the ZIF-8 powder while the ZIF-7 membrane showed the corresponding FTIR bands of the MOF powder. Characterization by XRD, FTIR, FIB, SEM, and STEM showed that these supported membranes were extraordinarily selective in the separation of H_2 and CO_2 containing binary mixtures with separation factors never previously reached in the case of ZIF-7. Thus, they were able to grow homogeneous, continuous, and thin layers of ZIF-7 and ZIF-8 with excellent stability using less amount of solvents.

Jeong et al. [67] have synthesized MIL-88A in a microfluidic device. This is to address limitations such as size control, architectural complexity, and functionalization. Iron (III) chloride, used as a metal precursor, and poly(vinyl alcohol) were dissolved in water to form the aqueous phase. While Fumaric acid (70 mM) was added in 1-octanol (nonpolar solvent) and sonicated in a water bath until a transparent solution was obtained and then, tributylamine (TBA) was added (105 mM) to form the organic phase. They introduced both the aqueous phase and the organic phase with a flow rate ratio of 1:5 by two separate syringe pumps into a microfluidic device. Droplets were created at T-junction and transferred to a perfluoroalkoxyalkane capillary. The continuous-flow droplets were transported into the microreactor coil for 5 - 20 minutes varied residence times at 40 ^{o}C. The obtained MOF crystals showed a typical spherical morphology with tunable size and uniform spherical shape (typically ca. 450 μm in diameter and ca. 2 μm in shell thickness). The XRD showed higher crystallinity at 15 minutes which indicated that the microfluidic strategy leads to a fast crystallization of MIL-88A. This result was attributed to better heat and mass transfer reached in the microfluidic environment.

Tanaka et al. [68] used a microfluidic system to study the competing roles of two kinds of ligands during nonequilibrium crystallization of $[Cu_2(pzdc)_2L]$ forming coordination polymers with pillared-layer structures (CPLs). The reagents (aqueous and continuous phase) were fed into a Y-shaped micro flow reactor with a 40^{o} confluence angle and 1 mm diameter by two syringe pumps and allowed to stand for 12 h. The resulting crystals were centrifuged, washed, and characterized. The SEM images showed that the particle sizes decreased with increasing concentration. They also discovered that the tube length and residence time has no effect on the particle size in their system. To study the effect

of flow rate, they altered the confluence angle of the microreactor to a Y-shape and arrow shape at 60^{o} and 300^{o}, respectively. The crystalline particle size was found to depend on the flow rate. The arrow-shaped reactor was found to produce larger particles for the same flow rate. This was attributed to the fact that a larger contact angle increases the mixing efficiency. The results of the analyses led to the confirmation that a microflow reactor is a valuable tool for evaluating non-equilibrium states, enabling the reaction solution to be observed directly and easier to study the complex mechanism.

Wang et al. [15] produced four types of Zr-based MOFs (MOF-801, MOF-804, DUT-67, and MOF-808) with different ligands and topologies as a pure phase of high-quality crystalline with uniform morphologies. They used a home-built microdroplet flow system consisting of three syringe pumps, a micro-mixer, heating, and a sample collection unit. Both the metal salt and organic ligands were pumped through the syringes into the micromixer. The magnetic stirrer in the micromixer ensured homogeneous mixing. Droplets were generated and passed through a heating coil with 2 mm i.d. 3 mm o.d. and 2 m in length. The microdroplets were then cooled, centrifuged, and washed. The PXRD analysis demonstrated a high purity sample with a degree of crystallinity higher than the solvothermal synthesis. The SEM images showed a uniform particle size of 300 nm for MOF-801 and MOF-808. MOF-801 and MOF-808 synthesized using the conventional solvothermal method exhibited inhomogenous dimensions with irregular shapes in the range of 2-3 μm and 3-5 μm respectively. MOF-804 and DUT-67 exhibited regular polyhedron crystals of 100-500 nm and 3-5 μm respectively. Despite the shorter retention time of 32-80 minutes under microfluidic conditions, all the crystals possessed higher purity and crystallinity than the conventional solvothermal method. This confirms the superiority of the microfluidic environment with a large surface-area-to-volume ratio, the efficient exchange of mass/heat, and the rapid recirculation of reactants during flow.

Table 2.1 Summary of MOF crystallization from solutions in microfluidic reactor systems

MOF	Molar Composition	Crystal Size	Pipe diameters (μm)	Residence time (min)	Flowrate (μL/min)	Temperature	Reference
MIL-88A	$FeCl_3.6H_2O$: PVA: Formaric Acid: TBA 2:0.7:1.05	450 μm	ID 500 OD 1600	20	(Q_d/Q_c) 1:5	40 °C	[67]
ZIF-8	$Zn(NO_3)_2$.6H2O: 2-N-methylimidazole+NaCOOH 1:3	3.67 ±0.9 μm	ID 315 OD 520	150	100	Room	[18]
ZIF-7	$Zn(NO_3)_2.6H_2O$: Benzimidazole + Ethanol 1:2	2.47 ±0.4 μm		100			
HKUST-1	$Cu(NO_3)_2.3H_2O$:BTC 1: 2.4	181 ± 32 nm	ID 1000	10,5,1	2000, 10000 and 20000	140 °C	[69]
UiO-66	ZrCl4: 1,4-tricarboxylic acid (BDC) 1:1	68 ± 14 nm		10	2000	130 °C	
NOTT-400	$Sc(SO_3CF_3)_3$: H_4BPTC 1:2	2.8 ± 0.910 μm		15	2000	85 °C	

2.7 Other Methods of Crystallizing MOF Precursor Solutions

Generally, MOF precursor solutions are crystallized from the liquid phase by mixing the ligands and the metal solutions in a suitable solvent. Temperature plays a vital role in the crystallization of MOF crystals from solutions. The temperature at which MOF is synthesized must be carefully chosen to suit a particular type of MOF desired or the

desired properties in the MOF to be synthesized. Other important factors that influence the nucleation and crystal growth of MOFs are reaction time, pH, metal ions, and organic ligands used, node size and their structural characteristics, the presence of counter ions, and the kinetics of the crystallization [66].

2.7.1 Batch Solvo (hydro)thermal Synthesis

A crystallization reaction that is carried out in a firmly closed container under autogenous pressure and above the boiling point of the solvent is termed Solvothermal Synthesis [70] and nonsolvothermal when it occurs below or at the boiling point under room temperature [71]. It is called Hydrothermal synthesis when the solvent is water. Most of the MOFs synthesized so far are under solvothermal conditions. Under this condition, temperature plays a vital role in the shape and morphology of the resulting MOFs. Perhaps, the major drawback of the traditional solvothermal process is the long hours or even days it takes to crystallize MOFs from the precursor solutions. Determining the exact reaction time is also essential as prolonged reaction time harms the MOFs, degrading the crystals and weakening the pores [71].

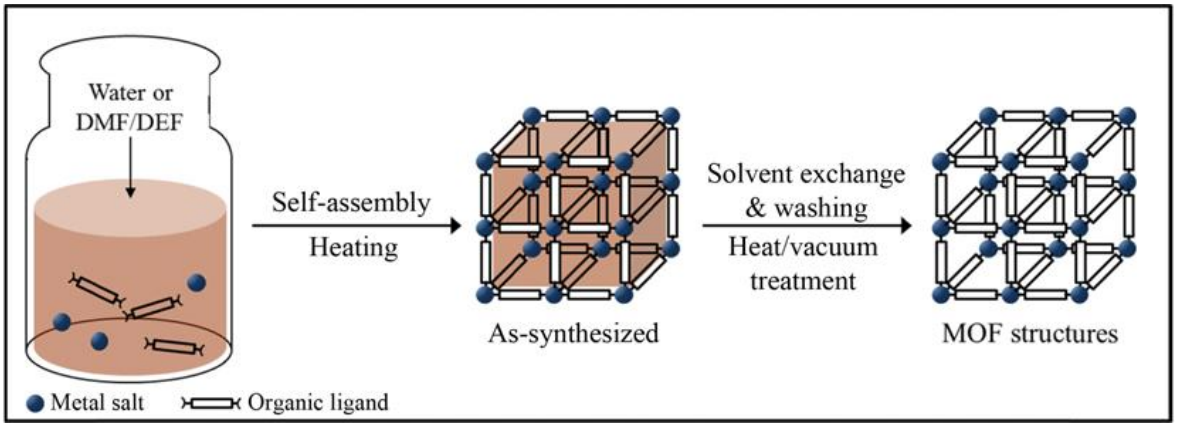

Figure 2.10. Conventional solvothermal Crystallization [26].

Leubner et al. [29] studied the impact of different solvents on MOF synthesis. They synthesized three different MOFs, CAU-10, Ce-UiO-66, and Al-MIL-53 using acetonitrile as solvent. Their main aim was to find an alternative solvent to synthesize MOF since N,N-dimethylformamide (DMF) which is a prominent solvent used to dissolve organic molecules (linkers) is considered hazardous and environmentally unfriendly. They carried out a solvothermal reaction of aluminum nitrate nonahydrate,

$Al(NO_3)_3 \cdot 9H_2O$, which is nearly insoluble isophthalic and terephthalic acid in acetonitrile at 130 ^oC for 23 h, which yielded CAU-10 or Al-MIL-53, respectively. For Ce-UiO-66, they reacted terephthalic acid with aqueous cerium ammonium nitrate $(NH_4)_2[Ce(NO_3)_6]$ solution in acetonitrile at 100 ^oC for 2 h. The products were purified and characterized. The powder X-ray diffraction (PXRD) patterns of CAU-10 and Ce-UiO-66 correspond well with theoretical patterns. However, the pattern of Al-MIL-53 was found to be more in line with V-MIL-47 [VO(BDC)] than the theoretical patterns of standard Al-MIL-53. The products were also used to carry out adsorption experiments and the calculated BET surface areas and pore volumes were well in line with the values reported in the literature. These results confirmed the successful synthesis of CAU-10, Ce-UiO-66, and Al-MIL-53 with acetonitrile which is considered less toxic than DMF. The structures of the three synthesized MOFs are shown in Fig. 2.11.

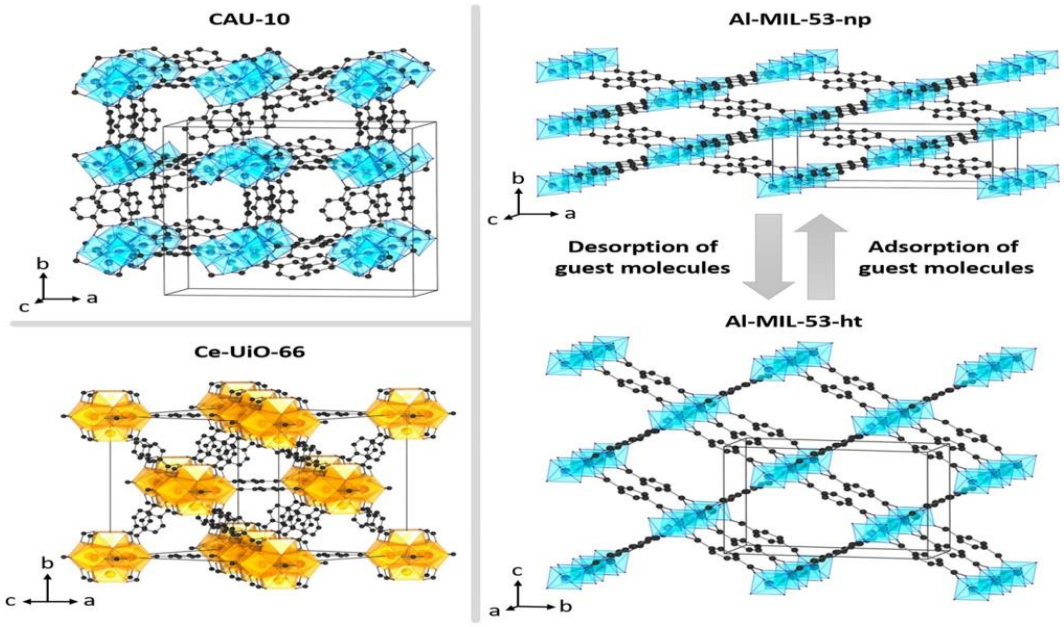

Figure 2.11 Structures of CAU-10 (top left), Ce-UiO-66 (bottom left), as well as narrow- (top right) and open-pore form (bottom right) of standard Al-MIL-53 with unit cell edges. [29].

Zhang et al. [28] carried out a study to show how solvents affect the formation and properties of MOFs. In their experiment, they synthesized $Cu_3(BTC)_2$ MOF by using a mixture of water/ethanol ratios of 0, 25%, 33%, 50%, 67%, 75%, and 100%. The organic linker (2.5mmol H_3BTC) and metal (2.5 mmol $Cu(OAc)_2.H_2O$) were dissolved separately

in the water/ethanol mixture and the two solutions were added under rapid stirring for 6 h at room temperature. The suspension was then centrifuged, and the precipitate was filtered and washed. The XRD analysis revealed that at a volume ratio of ethanol below 33% there was no MOF formation as a large amount of water prevents effective coordination between the carboxyl groups and the Cu atom. However, at a volume ratio of ethanol above 33% formation of crystalline $Cu_3(BTC)_2$ was observed. The morphologies of the crystals as revealed by SEM showed large crystals between 200–400 nm at a low ethanol ratio (33%). As the ethanol ratio reached 50% smaller crystals, ~60 nm was observed and continued to decrease as ethanol volume increased. Both the FTIR and thermogravimetric analyses support the MOF structure at ethanol volume concentration above 30 %. This study suggests strongly that the MOF crystal formation can be controlled by varying the solvent mixtures. It also shows that the formation and properties of $Cu_3(BTC)_2$ are strongly dependent on the strength of the hydrogen bonding between the solvent molecules and ligands.

A rapid solvothermal method to produce UiO-66 particles in a batch system, which took about 30 minutes, was applied by Bae et al. [72]. They dissolved 1.06 g of zirconium (IV) chloride ($ZrCl_4$) and 0.78 g of 1,4 benzene dicarboxylic acid (BDC) separately with 30 ml dimethylformamide (DMF). They repeated this procedure both by halving and doubling the concentration of the precursor solution to study the effect of precursor concentration on the resulting synthesized MOF structures. The solutions were mixed and transferred into autoclaves and placed in an oil bath at 80, 100, 120, and 140 ^oC for 30 min. The solutions were then cooled at room temperature for 2 h, centrifuged to separate the resulting UiO-66 particles, washed several times with ethanol, and finally dried at 70 ^oC overnight. The XRD pattern for UiO-66 synthesized at different precursor concentrations did not follow any particular trend, as the one with the typical precursor concentration showed the highest peak and the sample with half the concentration showed the lowest level of crystallinity, while the sample with the double concentration showed a moderate level of crystallinity. This result was possibly due to the synergetic balance of precursors that was needed in the formation of UiO-66 crystals. They argued that the synergy, the $Zr_6O_4(OH)_4$ inner core that was initially a regular highly packed face-centered cubic structure was thought to undergo a continuum of truncations into the finally rectified form of a polyhedron during nucleation and crystal growth. The edges of this polyhedron were then bridged by the carboxylates originating from the dicarboxylic

acid, while the Zr atom was bonded with the ligands through the oxygen atom supplied by the carboxylates. The SEM images indicated that the particle size decreases with the increasing concentration of precursors. The XRD pattern of the samples prepared at different temperatures showed that the higher the temperature the higher the peak intensity up to 120 ^{o}C. Increasing the synthesis temperature to 140 ^{o}C resulted in more or less similar peak intensity. The morphology of UiO-66 prepared at various synthesis temperatures, and analyzed via SEM images showed that the particle size increased with well-formed shapes as the temperature increased. This was explained that, at high temperature and low-pressure conditions, the solubility of the colloid system typically increases, thereby facilitating further growth of the particle. They concluded that the UiO-66 prepared using the method proposed was found to be favorable for deployment in the industry due to the shortened route of synthesis.

2.7.2 Microwave-Assisted synthesis

Microwaves (MW) are a form of electromagnetic radiation with frequencies between 300 and 300 000 MHz. Microwave synthesis has the advantages of fast crystallization, phase selectivity, narrow particle size distribution, and facile morphology control [26]. As shown in Figure 2.12, in this method, energy for the reaction is supplied by microwave in the form of radiation which is used to activate a point of contact between electromagnetic waves and mobile electric charges of different polarities in a solid or liquid state [26, 27]. Just like in all synthetic methods, microwave-assisted synthesis imposed additional criteria on the choice of solvent. A suitable solvent must be able to absorb microwave energy and convert electromagnetic energy into heat. This is determined by dielectric loss tangent, as a larger value of dielectric loss tangent favors the efficient conversion of microwave energy into heat.

$$tan\delta = \frac{\varepsilon''}{\varepsilon'} \qquad (2.12)$$

where stands for dielectric losses and is the relative permittivity [65]

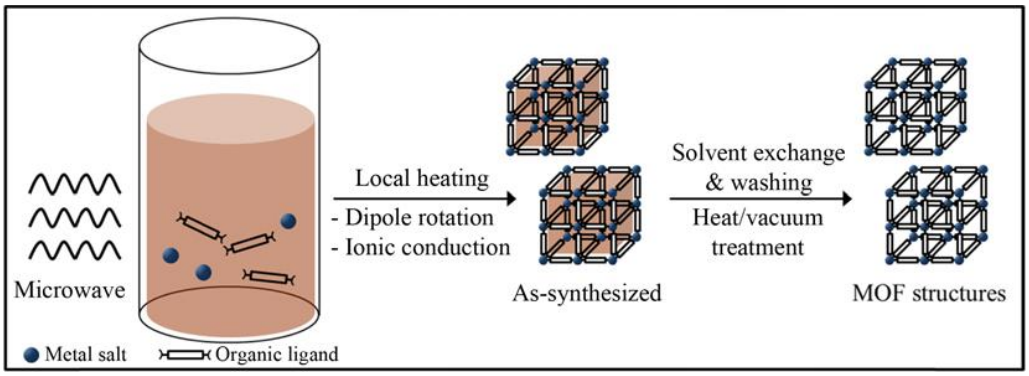

Figure 2.12. Microwave-assisted solvothermal synthesis of MOF structures [26].

2.7.3 Sonochemical Synthesis

The term ‘’sono’’ means sound. The sonochemical process involves molecule transformation under high-energy ultrasonic radiation (20 kHz–10 MHz). The reaction solution is irradiated with ultrasound radiation forming bubbles, which in turn create local hot spots of a short life with a high temperature and pressure leading to chemical reactions and the formation of crystallization nuclei [27]. A typical experimental setup for the sonochemical synthesis method is shown in Figure 2.13.

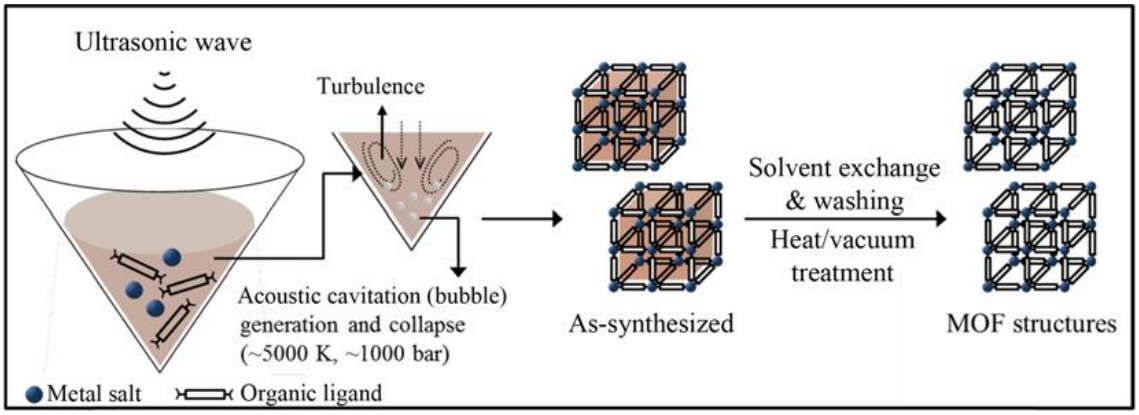

Figure 2.13 Sonochemical synthesis of MOF structures [26]

Son et. al synthesized MOF-5 by application of the sonochemical method using 1-methyl-2 pyrrolidone (NMP) as a solvent, achieving a faster crystallization occurring within 8-30 mins compared to 12 – 24 hr synthesis time for solvothermal synthesis. In addition, the average size of the sonochemically synthesized MOF-5 was 5–25 mm, which is approximately 60 times smaller than solvothermally synthesized MOF-5 (ca. 900 mm) on average [73]. In a similar study, Jung et. al synthesized MOF-177 by the sonochemical process with 1-methyl-2 pyrrolidone (NMP) as a solvent. The crystal sizes were found to

be smaller (5 - 20µm) in 40 mins than those synthesized by microwave (5 – 50 µm) in 35 mins with less crystallinity, and the conventional solvothermal method (0.5–1.5 mm) in 48 hrs. Also, the product yield of 96.5% achieved through the sonochemical route was found to be significantly higher than other methods [74].

2.7.4 Electrochemical Synthesis

In this method, metal ions are generated by the electrochemical route. It is commonly used for industrial-scale production of MOF powder [27]. Here, instead of using metal salt, the metal ion is provided by anodic dissolution into reaction mixtures that contain the organic ligands, and electrolytes as shown in figure 8. Compared to the solvothermal method, this method has the advantage of lower temperature and faster synthesis. The risk of metal deposition on the cathode is avoided using protic solvents but hydrogen is generated.

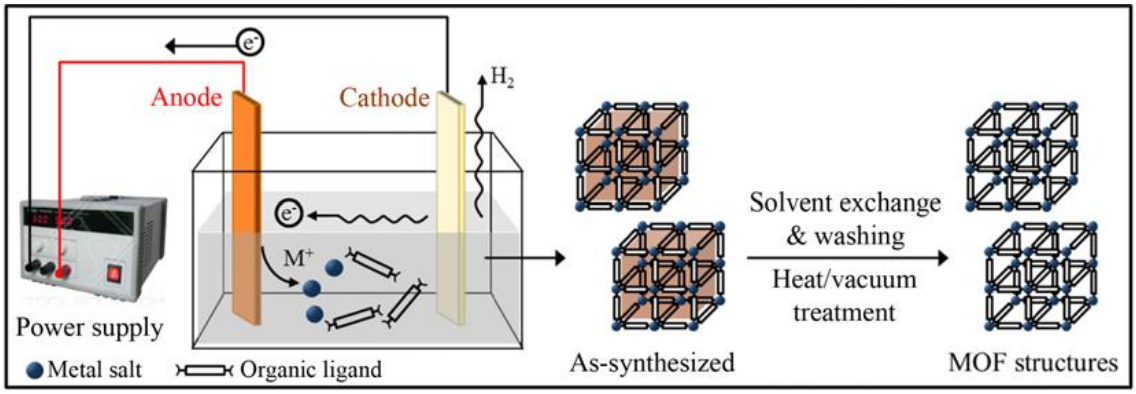

Figure 2.14. Electrochemical syntheses of MOF Crystallization [27].

According to Joaristi et. al, the general advantages of this method are the shorter synthesis time, the milder conditions, the facile synthesis of MOF nanoparticles, the morphology tuning, and the high Faraday efficiencies than the conventional solvothermal or microwave synthesis. They demonstrated the robustness of the electrochemical method in the synthesis of porous materials by synthesizing HKUST-1, ZIF-8, MIL-100(Al), MIL-53(Al), and NH2-MIL-53(Al) via anodic dissolution in an electrochemical cell. They pointed out the drawback associated with this method, that it seems to be limited to a situation where instantaneous nucleation is possible. This explains why MIL-53 and NH2-MIL-53 samples exhibit suppressed framework flexibility compared to samples

synthesized solvothermally, and therefore, there is a need for enhanced synthesis conditions for MOFs such as MIL-53, MIL-100, or ZIF-8 [75].

2.7.5 Mechanochemical Synthesis

Mechano-chemical method, as evident from the name, involves the hybrid of mechanical and chemical processes for the synthesis of Metal-Organic Frameworks (MOFs). The mechanical process involves applying mechanical force to the breaking of intramolecular bonds by either manual grinding of the reagents or in automatic ball mills and the subsequent transformations that follow involve the chemical aspect. A typical setup is shown in Figure 2.15. This method is environmentally benign as it requires no organic solvent. Another advantage is that MOFs can be synthesized at room temperature. These features lead to a short reaction time (10 – 60 min) which has a great influence on the resulting MOFs, especially the yields and crystal size. The drawback associated with mechanochemical synthesis is its high selectivity and therefore, it can only be applied to specific MOF types only [27]. Currently, there is no general theory explaining physicochemical processes that occur in mechanochemical reactions [65].

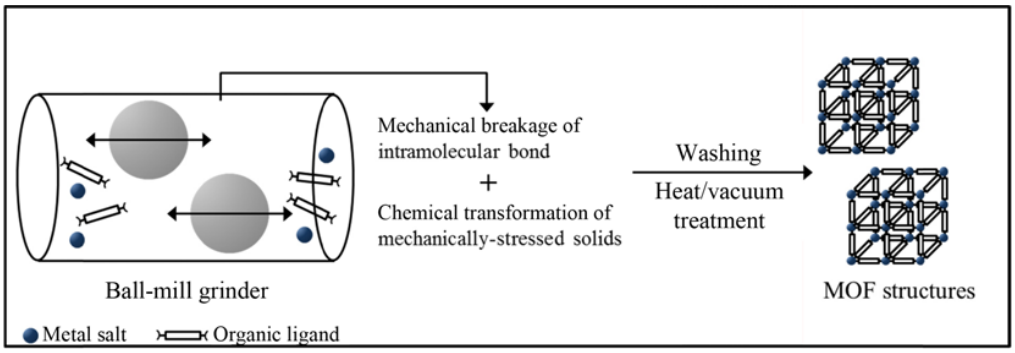

Figure 2.15. Mechano-chemical synthesis of MOF crystallization [27].

3. MATERIALS AND METHODS

3.1 Materials

3.1.1 Microfluidic Device

The microfluidic device used in this study was designed by Dr. Selis Önel as part of her research at the Center for Engineering in Medicine and Surgery (CEMS) and the BioMEMS Research Center associated with Harvard Medical School and Massachusetts General Hospital (MGH).

The device consists of four parts. The microfluidic device is meant to confine the precursor solution and oil to a narrow environment and generate picoliter droplets at the X-junction (Figure 3.1b). The inlet region consists of three ports (Figure 3.1a). The middle port (Continuous phase inlet) divides into two divergent paths and reconnects at the X-junction together with inner ports where the droplet is generated, known as the droplet formation region (Figure 3.1b). The outer port (Auxiliary oil inlet) also divides into two divergent channels and connects the other two at the Y-shaped junction (figure 3.1c). The purpose of the auxiliary is to control the distance between the droplets. The channel continues with a wider diameter, denoted as the auxiliary oil region. The auxiliary oil region extends to the serpentine, where intense mixing and heating are applied, and finally, to the outlet port. The serpentine consists of 24 parallel channels. These parallel channels have a width of 400 μm, and the parallel-row channels are interconnected by U-turn channels of the same width. The purpose of the serpentine zone is to prolong the residence time of the droplets (precursor solution) in the channel for nucleation to take place.

All the processes taking place at the various sections of the microfluidic device are observed under an inverted microscope (Olympus IX73). Figure 3.2 shows the 3D printed holder designed to provide a firm grip for both the ITO heater and the microfluidic device onto the microscope to avoid slipping, and prevent the tubes from touching each other. The device also has two thermocouple inlets through which the required temperature is regulated.

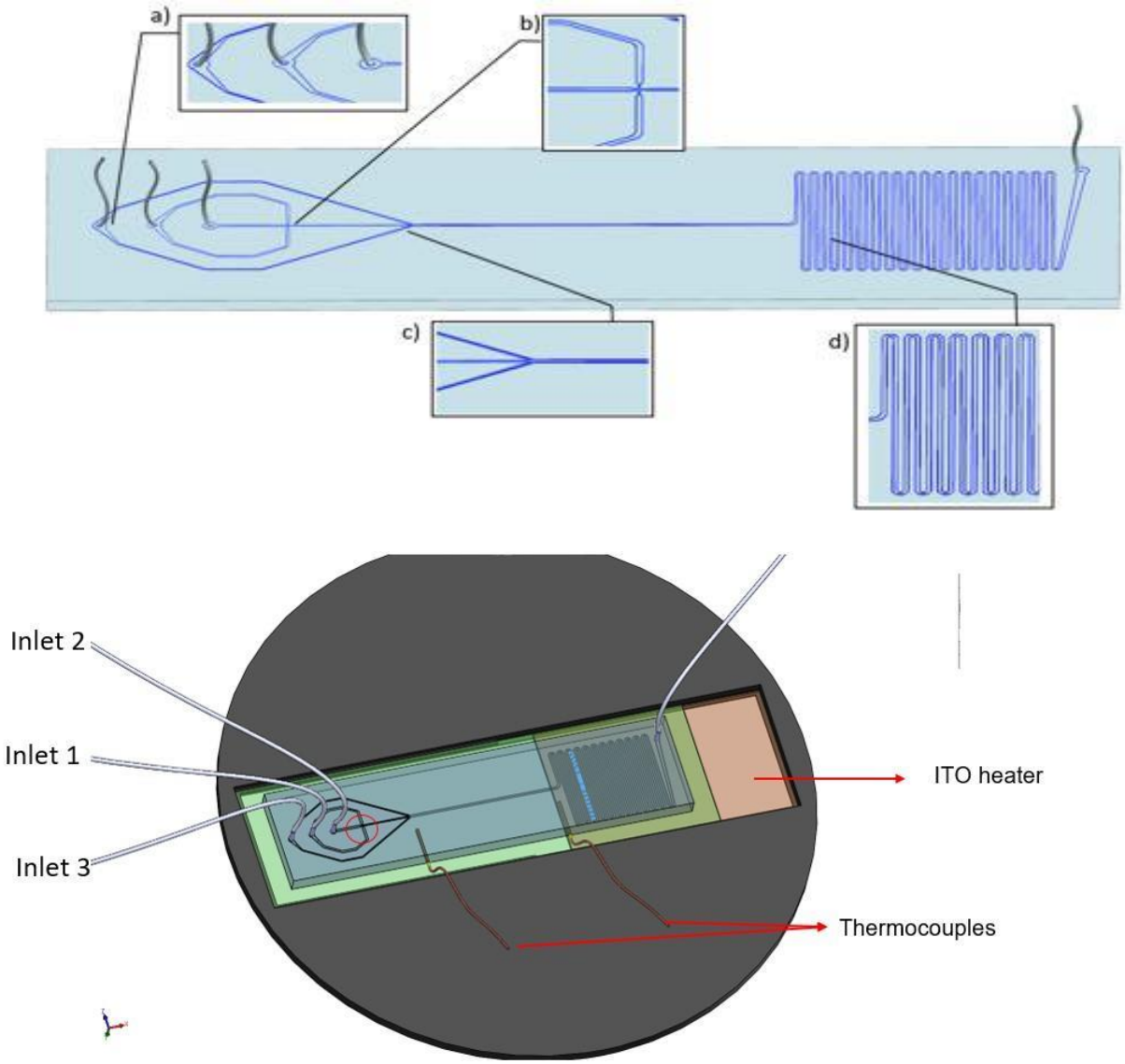

Figure 3. 2 PDMS Microfluidic Device [76]: a) shows the inlets through which oils and UiO-66 precursor solutions (dispersed phase) are injected into the microfluidic devices. b) is known as a droplet generation junction. This is the point where oil (the continuous phase) combines with the dispersed phase to generate droplets. c) is the point where the auxiliary oil joins the flowing droplets, known as the auxiliary junction. d) is the serpentine region, where heat is applied and nucleation of the precursor solution takes place.

Figure 3. 3 Microfluidic device mounted on 3D printed holder with thermocouples and the heater [77]. Inlet 1 delivers oil (continuous phase) into the microfluidic device while

inlet 2 and inlet 3 deliver oil (auxiliary phase) and UiO-66 precursor solution (dispersed phase) respectively.

3.1.2 Fabrication of Microfluidic Device

Polydimethylsiloxane (PDMS) material was used for the production of microchannel devices, as it is transparent and resistant to the temperatures to be used. Device molds with microchannels were produced by the photolithography method by coating photoresist SU-8 material on the silicon wafer. For this, chrome-glass masks in which the device geometry is processed by the photolithographic method are used. Transferring the microchannel geometry onto the PDMS material was done by soft lithography. In this method, the viscous polymer solution formed by mixing PDMS (Sylgard 184; Dow Corning, Midland, MI) and cross-linking agent (curing agent) at a ratio of 10:1 is poured into the SU-8 mold. Air bubbles trapped in the mold were removed in the vacuum environment using a desiccator for 1 hr. The hardening process is carried out via cross-linking by curing in an oven at 80 oC for 1 hr. The mold together with the cured PDMS device was removed from the oven and left to cool at room temperature. The PDMS device was then removed from the SU-8 mold using a surgical knife. The channel inlets and outlet ports were drilled using 75 gauge needles (punch). The PDMS and a glass slide were washed to remove dirt from the surface and dried in the oven in preparation for plasma bonding. The PDMS device containing the channels and a glass slide is exposed to plasma (Harrick Plasma Inc. PDC 32G-2 Model) for surface cleaning and bonding, with the surface to be bonded facing up. The plasma was adjusted until the color of the internal environment is neither purple nor blue. The knob was then set to high. The PDMS device and a glass slide were exposed for 50 seconds (Figure 3.3). The PDMS and the glass slide were removed and bonded together as fast as possible to take their final shape. The device was left in the oven overnight for complete bonding. Figure 3.3 Vacuum Plasma activation setup for microfluidic device fabrication.

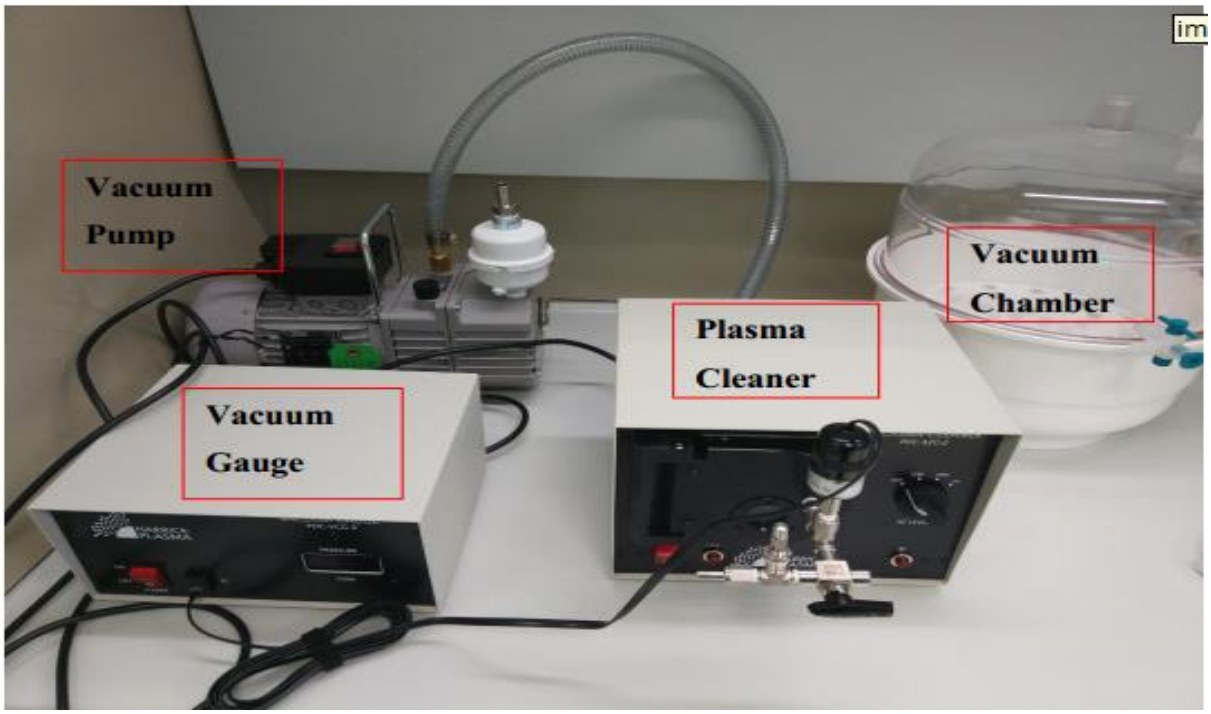

Figure 3. 4. Vacuum Plasma activation setup for microfluidic device fabrication

3.1.3 Preparation of Solutions

A two-phase microfluidic system requires two immiscible liquids to generate droplets. These two liquids are named aqueous and continuous phases. In this work, the precursor is the aqueous solution, otherwise known as the dispersed phase. Silicon oil was used as the continuous phase because it preferentially wets the hydrophobic surface of the Teflon tubing, thereby producing a continuous phase for the MOF precursor mixture to travel as discrete, uniformly spaced droplets within the tube [78]. All chemicals were obtained commercially (Sigma Aldrich, Boston) and used without further purification. The properties of the continuous and dispersed liquid phases used in the study are given in Table 3.1. For the UiO-66 precursor solution, the recipe was obtained from Prof. Dr. Burcu Akata Kurç's laboratory at Middle East Technical University. A solution with 19 mM $ZrCl_4$ and 32 mM H_2BDC concentration was prepared. 0.067 g of zirconium (IV) chloride ($ZrCl_4$) and 0.09 g of 1,4-benzenedicarboxylic acid (BDC) were dissolved in two separate reagent bottles containing 5 ml and 10 ml of N,N-dimethylformamide (DMF), respectively. Here the DMF serves as the solvent for both the metal salt ($ZrCl_4$) and the organic linker (BDC). The bottles were shaken and both solutions were placed in a water bath sonicator for 20 min for complete dissolution. The acid solution was added to the zirconium salt solution and the mixture was sonicated for another 20 min to achieve a

homogeneous solution. This solution was prepared at the laboratory of Dr. Burcu Akata Kurç at Middle East Technical University.

Table 3.1 Properties of the materials that make up the dispersed phase and the continuous phase

UIPAC Name	Molecular Formula	Physical state	Crystal structure	Molecular weight (g/mol)	Polarity	Density (g/cm^3)	Viscosity (cSt)	Surface Tension (mN/m)
Dimethylformamide	DMF (C_3H_7NO)	Liquid	Triclinic	73.09	Polar	0.944	0.757	36.42
Zirconium chloride	$ZrCl_4$	Solid	Monoclinic	233.04	Nonpolar	2.8	N/A	N/A
Terephthalic acid	H_2BDC'(98%) (C_6H_4-1,4-$(CO_2H)_2$)	Solid	Triclinic	166.13	Nonpolar	1.58	N/A	N/A
Silicone Oil	[-$Si(CH_3)_2O$-]$_n$	Liquid	N/A	N/A	Nonpolar	0.968	1000	21.1

3.2 Experimental Methods

3.2.1 Experimental Setup

The complete experimental setup of the flow-focusing two-phase microfluidic system is made up of the following components (Figure 3.4). Computer-controlled Nemesys BASE120 (CETONI GmbH), controls the syringe pump to deliver liquids to the PDMS device based on the given flow rates. Teflon tubings, through which the solution and oil flow into the PDMS microfluidic device. The microfluidic device, where droplets are generated and eventually crystallize as the droplets are heated and travel through the serpentine. PID controlled indium-tin-oxide (ITO) heater and its controller (Cell MicroControls, Norfolk, VA) and Olympus IX73 inverted microscope with a DP73 high-speed camera for live monitoring of the experiment.

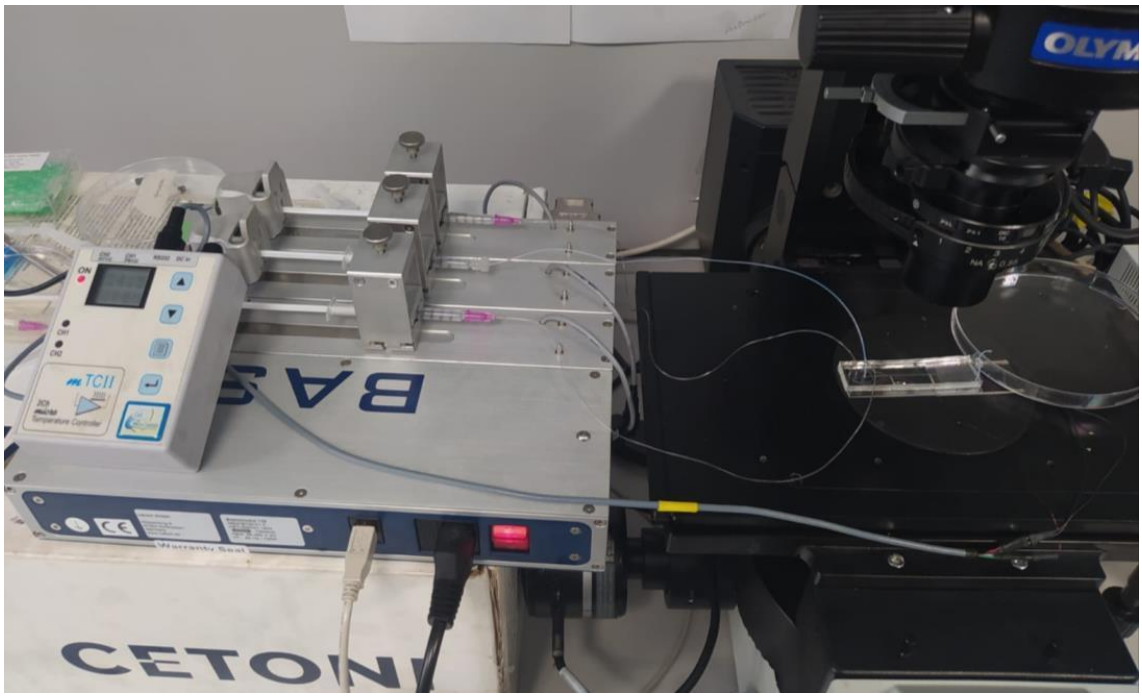

Figure 3. 5 Complete Experimental Setup.

3.2.2 Optimization Of Droplet Generation

The optimization experiment was carried out to better understand the system and establish the relationship between the dispersed phase and the continuous phase with droplet sizes, as well as interdroplet distances. Although, the flow-focusing microfluidic system was originally designed to generate droplets at a flow rate ratio of 20:1 for the continuous phase and the dispersed phase respectively. However, droplet size changes as the flow rate were varied. In Figure 3.4, the syringe pumps on the left and right contain silicone oil as a continuous phase while the middle syringe contained UiO-66 precursor solution (ZrCl4 + BDC dissolved in DMF). The solution and oil were fed into the syringe pumps. The syringe pumps were calibrated through the Computer-controlled Nemesys BASE120 (CETONI GmbH). The syringe pumps were firmly tightened, but carefully to ensure that they are not distorted, but stand horizontally. This is to avoid unnecessary pressure drops and deliver the correct flow rate through the Teflon tubings to the PDMS microfluidic device. The optimization experiment was in two parts. Optimization was done from the droplet generation region (henceforth referred to as the cold region) to just before they entered the serpentine, where heat was applied (henceforth referred to as the hot region).

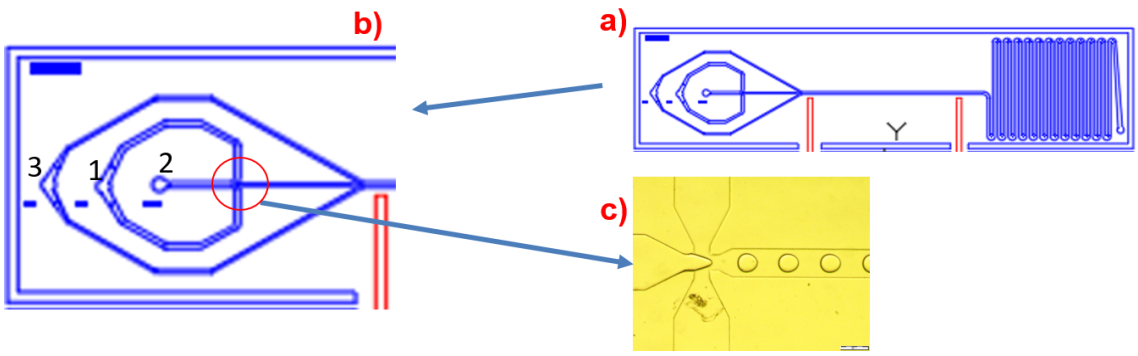

Figure 3. 6. General view of the microfluidic device used in the studies, inlet ports, and a zoomed-in view of the droplet formation region (c).

3.2.2.1 Optimization Of Droplet In The Cold Region

The starting flow rates were set at 2 µL for the three syringe pumps. A stepwise reduction of the dispersed phase (UiO-66 precursor solution) by 0.2 was adopted. For each reduction in the flow rates of the dispersed phase, a waiting period of 2 min was adopted to ensure the stability of the flow. The middle syringe in figure 3.4 delivered the precursor solution (dispersed phase) through Teflon tubing to the inlet ports 2 (figure 3.5b) of the PDMS microfluidic device which combine with the silicone oil from port 1 at the X-junction to generate droplets. The average droplet size and interdroplet distances were measured at three different points for every change in the flow rate of the dispersed phase. As shown in figure 3.5, the measurements were taken at the droplet generation region immediately after the precursor solution and silicone oil were combined at the X-junction to generate droplets (Figure 3.5c). With the simultaneous video or images taken from these regions at different flow rates, diameter measurements and distance between droplets for at least five droplets were measured. Average droplet and average interdroplet distance values for each region were taken. Next measurements were taken at the auxiliary region after the droplets had passed through the second junction (Y-junction) to flow in the auxiliary oil (Denoted as Y in Figure 3.5a). The final measurements were taken at the heating region just before the droplets entered the serpentine.

The average droplet sizes and interdroplet distances measured were rendered dimensionless by dividing by the hydraulic diameter (D_h) of the microfluidic device using equation 3.1.

$$D_h = \frac{2*h*d}{h+d} \qquad (3.1)$$

Where *h* is the height of the channel (100 µm everywhere) and *d* is the channel diameter (200 µm for a1 region and 400 µm for b1, b2, and serpentine regions).

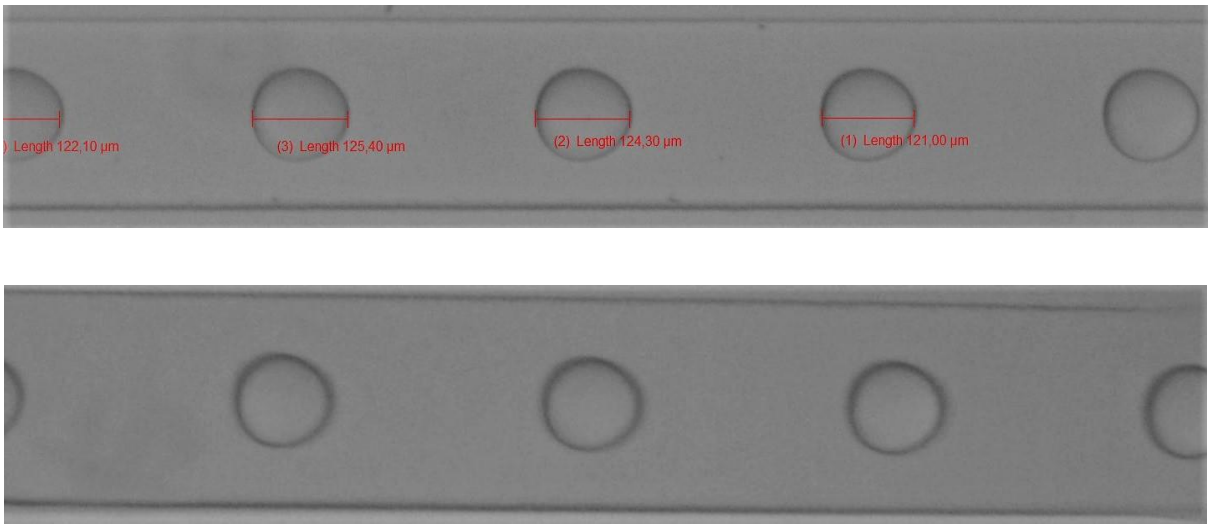

Figure 3. 7 Examples of Droplet measurements at different sections of the device.

3.2.2.2 Optimization In the Hot Region

Optimization was done to determine how droplets shrink from the point heat was applied until nucleation was observed as the droplets traveled through the serpentines. The temperature was kept constant at 80 ^{o}C, and the optimization was carried out at different droplet sizes (70, 90, and 110 µm) by varying the flow rates accordingly. Droplet sizes were measured from the pictures taken at the same location in each serpentine as the droplets advanced until nucleation was observed in the serpentine.

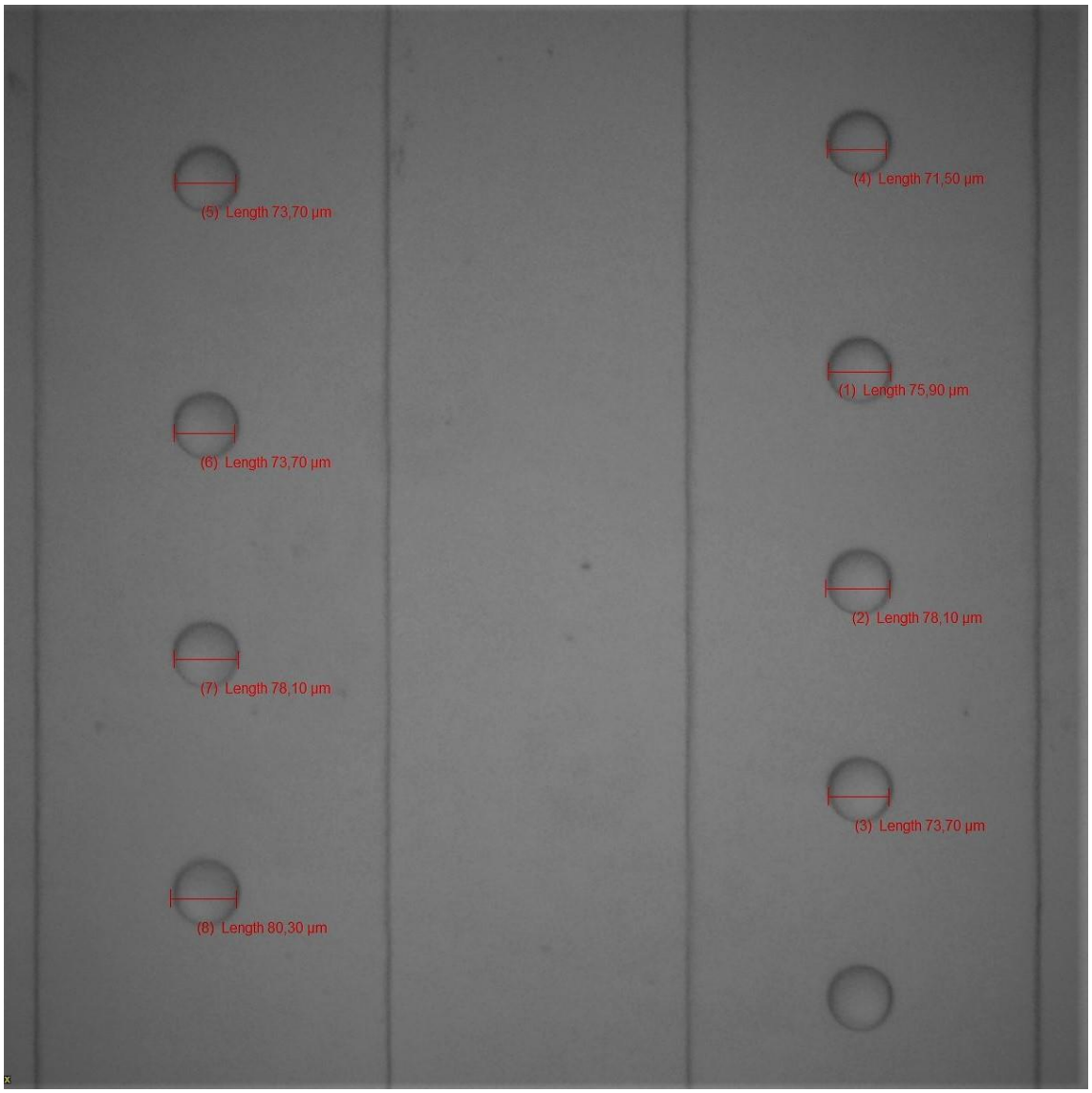

Figure 3. 8. Droplet measurements being taken at the serpentine section

3.2.3 Crystallization Experiment

The crystallization experiment was conducted in the two-phase flow microfluidic system to get the nucleation point in the microfluidic device out of the precursor solution. The generated droplets were controlled to achieve the desired droplet size by varying the flow rate. The desired droplet size was measured at the heating region. The heating device was then set to the desired nucleation temperature and allowed to pass through the serpentine until nucleation was observed. The point where nucleation occurred was noted and the number of droplets that nucleated at that point.

3.2.3.1 Effect of Droplet Size on the Nucleation Time

Crystallization of the precursor solution was carried out at three different droplet sizes. Here the temperature was kept at 80 ^{o}C while the crystallization experiments were carried out for droplet sizes of 70 μm. As the droplets traveled through the serpentine, the first point of nucleation within the serpentine was noted and the time taken from the heating region to the point of nucleation was calculated (see Appendix 3-5). The same procedure was repeated for 90 and 110 μm. The generated droplets and the nucleation processes were monitored live with an Olympus IX73 brand inverted microscope, and the microscope images were analyzed in a computer environment by using the Stream Motion program.

3.2.3.2 Effect of Temperature on the Crystallization of UiO-66 Precursor Solution

Crystallization of the supersaturated solution was carried out at three different temperatures. Here a droplet size of 70 μm was kept constant while the temperature was varied (50, 80, and 100 ^{o}C). A 15-second interval was adopted to count the number of droplets that nucleated at that point for each temperature. The time taken to reach the nucleation point was calculated (see Appendix 6-8) and the number of droplets observed to have nucleated was used to calculate the kinetic behavior of the crystallization process in the droplet-based two-phase microfluidic system. These processes were repeated 3 times and obtained results are the average of the data collected. The generated droplets and the crystallization processes were monitored live with an Olympus IX73 brand inverted microscope, and the microscope images were analyzed in a computer environment by using the Stream Motion program.

During the whole experiment, crystals sometimes stick to the wall of the channels in the serpentine, hindering the smooth movement of flow, especially at high temperatures, or droplets catching up with one another and coalescence, especially at large droplet sizes as shown in Figure 3.6. when any of these happened the flows were stopped, the heating device switched off and the flow rates were increased to allow large droplet sizes to flow through the serpentine and pushed the sticking crystals to the outlet, thereby cleaning the channels.

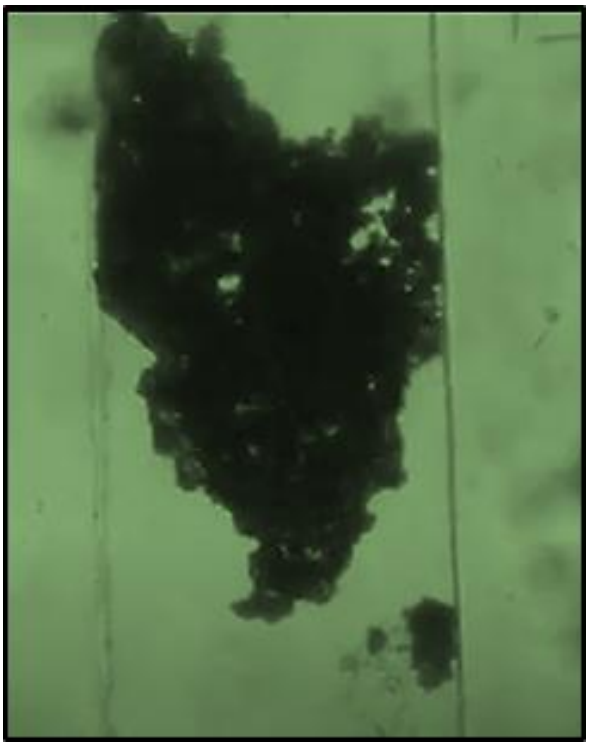

Figure 3. 9. Crystals stick to the wall of the channels during crystallization.

3.2.4 Kinetic Model Calculations

The classical nucleation theory (equation 3.2) was implemented in determining the kinetic parameters at the three nucleation temperatures (50, 80, and 100 ^{o}C). In this work, droplets shrank until it reaches enough supersaturation and nucleated. Hence *J is* referred to as the rate of droplet nucleation here, so as not to confuse it with a system where many nuclei are observed within a particular volume of droplets. Supersaturation, which is the driving force for nucleation, is defined as a ratio of initial concentration (C) to equilibrium concentration (C*). The rate of droplet nucleation is given by:

$$J\ (s^{-1})\ = k_N \exp\left(\frac{-16\pi\gamma^3 V_m^2}{3(KT)^3(lnS)^2}\right) \qquad (3.2)$$

where J is the droplet nucleation rate (s^{-1}), γ is the interfacial tension between the crystal and solution (N/m), V_m is the molecular volume of the crystallizing molecule (m^3/mol), k is the Boltzmann's constant (1.38 x 10^{-23} JK^{-1}), and T is the absolute temperature (K). S is the relative supersaturation ratio given by:

$$S = \frac{C}{C^*} = \frac{V_f}{V_i} \qquad (3.3)$$

where V_f and V_i are the initial and the final volume, respectively.

Many nuclei might be forming all at once and then coalescing into one particle, but the fast kinetics taking place in the droplet during the formation of a solid cannot be visualized with the optical microscope and camera used. Therefore, nucleation of one crystal per droplet is assumed. The number of droplets (N) that nucleated at time t, i.e. the time taken from the heating region to the point in the serpentine where nucleation was observed, was counted from the motion picture taken and divided by time to give the rate of nucleation as shown below:

$$\text{J}\ (\text{s}^{-1}) = \frac{\text{Number of nucleated droplets (N)}}{\text{Nucleation time (s)}} \quad (3.4)$$

k_N in equation 3.2 is the kinetic constant of nucleation and has Arrhenius temperature dependency given by:

$$k_N(T) = k_0 \exp\left(-\frac{E_N}{RT}\right) \quad (3.5)$$

where E_N (Jmol^{-1}) is the activation energy for nucleation and R (J.mol^{-1}.K^{-1}) is the gas constant.

From equation (3.2);

$$lnJ = lnk_N - \left(\frac{16\pi V_m^2 \gamma^3}{3k^3} \frac{1}{T^3(lnS)^2}\right)$$

lnJ was plotted against $\frac{1}{T^3(lnS)^2}$ and the slope of the curve was substituted into equation 3.2 to model the rate of nucleation in the microfluidic system used in this work at the temperatures under consideration. The nucleation rate constants (k_N) were, therefore, calculated for each temperature.

In the same vein, equation 3.4 was linearized as:

$$lnk_N(T) = lnk_0 - \frac{E_N}{R} * \frac{1}{T}$$

lnk_N was plotted against $\frac{1}{T}$ and the activation energy for nucleation was calculated from the slope ($\frac{E_N}{R}$) and intercept gave k_0

4. RESULTS AND DISCUSSION

4.1 Optimization of Droplet Generation in the Cold Region

Optimization of droplet generation was done by manipulating the flow rate ratio of dispersed and continuous phases to generate the different sizes of droplets and interdroplet distances. Since the droplets are obtained to serve as picoreactors, it is very important to generate droplets of equal sizes, to stay apart while advancing in the channels and not coalesce, and for the residence time in the channels to be optimally adjusted for nucleation and crystal formation with similar quality characteristics. The optimization was aimed to determine the operating limits of the microfluidic system depending on the characteristics of the continuous phase (silicone oil) and the dispersed phase (UiO-66 precursor solution) of the two liquids supplied to the device and to determine what flow rate gives a particular droplet size and interdroplet distance. Flow rates must, therefore, be adjusted properly.

4.1.1 Optimization of Droplet Generation in the Cold Region

It can be seen in Figure 4.1 that, as the flow rate ratio of dispersed and continuous phases (Qd/Qc) decreased due to a 0.2 stepwise decrease in the flow rate of the dispersed phase, the droplet sizes were reduced. As the droplet sizes reduced, interdroplet distances increased (Figure 4.2). Depending on the flow rates, jet flow, droplet formation, or reflux of the dispersed phase (failure to pass through the first connection point) were observed. At the early stages of the experiment when the flow rates of dispersed and continuous phases were closed jet flow was observed (Appendix 2) until when the dispersed phase flow rate was 1.4 µL/min corresponding to a flow rate ratio (Q_d/Q_c) of 0.7.

Another interesting point to note is that as the flow rate ratio reduced the droplets became more spherical, reduced in size, and distances between the droplets becomes more pronounced and orderly. This is expected since a reduction in the flow rate of the dispersed gives the continuous phase (silicone oil) more power to cut the dispersed phase into discrete droplets. So, the lower the flow rate of the dispersed phase (precursor solution) the more the continuous phase (silicone oil) can encircle the dispersed phase and has more control in producing the monodispersed droplets with spherical shapes.

The curves in Figure 4.1 show that the changes in the flow rate ratio (Qd/Qc) do not give proportionate changes in the droplet sizes. It was also observed that as the droplets were progressing along the channel they became smaller in size, more spherical, and flow became stable even without changing the flow rate of both phases. More shrinkage occurred at the second junction (b1) when the auxiliary oil joined the flow. This could be due to additional pressure exerted on the droplet at the junction and the flow rate of the auxiliary oil.

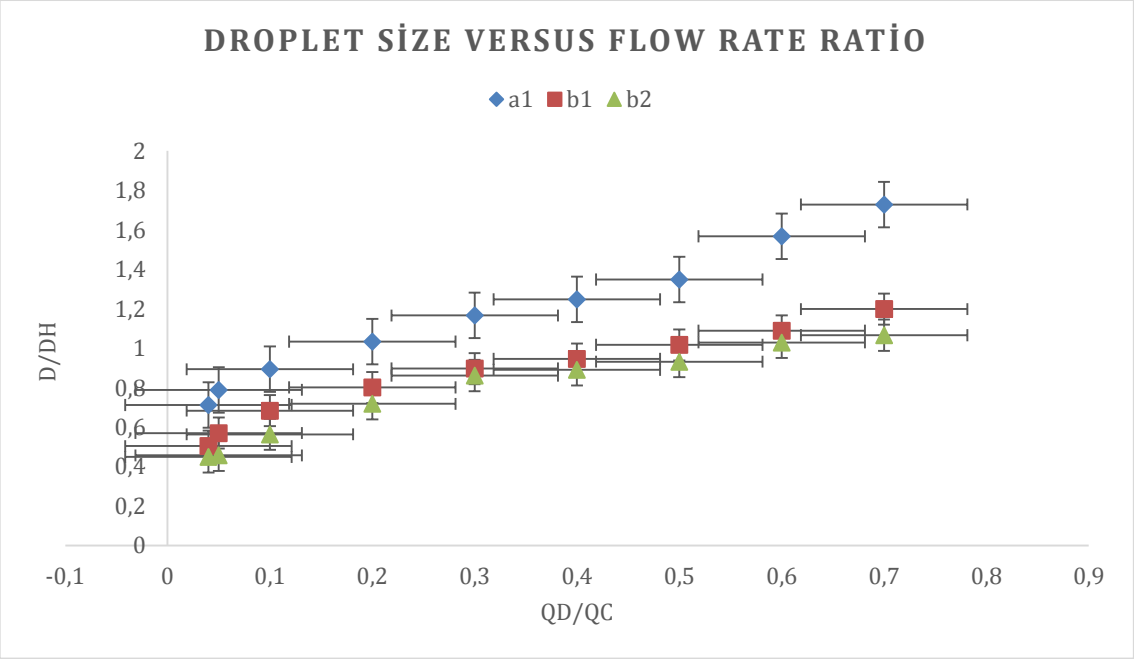

Figure 4. 1. Relationship between the size of the droplets and the ratio of flow rates (Qd/Qc): a1 shows the average droplet sizes measured at the droplet generation junction, b1 shows the average droplet sizes measured at the auxiliary junction and b2 shows the average droplet sizes measured just before the droplets entered the serpentine.

Figure 4.2 shows that interdroplet distance has an inverse relationship with the flow rate ratio Qd/Qc. This is expected due to the conservation of mass or the continuity equation. The droplets are expected to be larger for constant frequency of formation or the frequency of fomation will increase for constant droplet size as the amount of precursor solution increases while the amount of oil per time is kept constant. The surface-to-surface distance between the droplets will decrease in both cases. This is also supported

by the observation of the fact that as the droplet sizes reduced during their progress along the channel, the distance between them became wider. A critical look at the figure also shows the lines were more smooth at b1 and b2 than they were at b1. This is because at the formation of the droplets the molecules of the components of the solution may be more agitated, and tend to move in a more zig-zag manner. It also shows that as the droplets became smaller and more spherical they tend to maintain a smooth course of flow with relatively equal distances apart. Thus, this shows the importance of optimization of the droplet generation in the microfluidic system to be able to deliver the desired droplet size to the heating region and maintain a reasonable distance between the droplets to avoid coalescence as they flow in the auxiliary oil phase into the serpentine where nucleation is expected to take place.

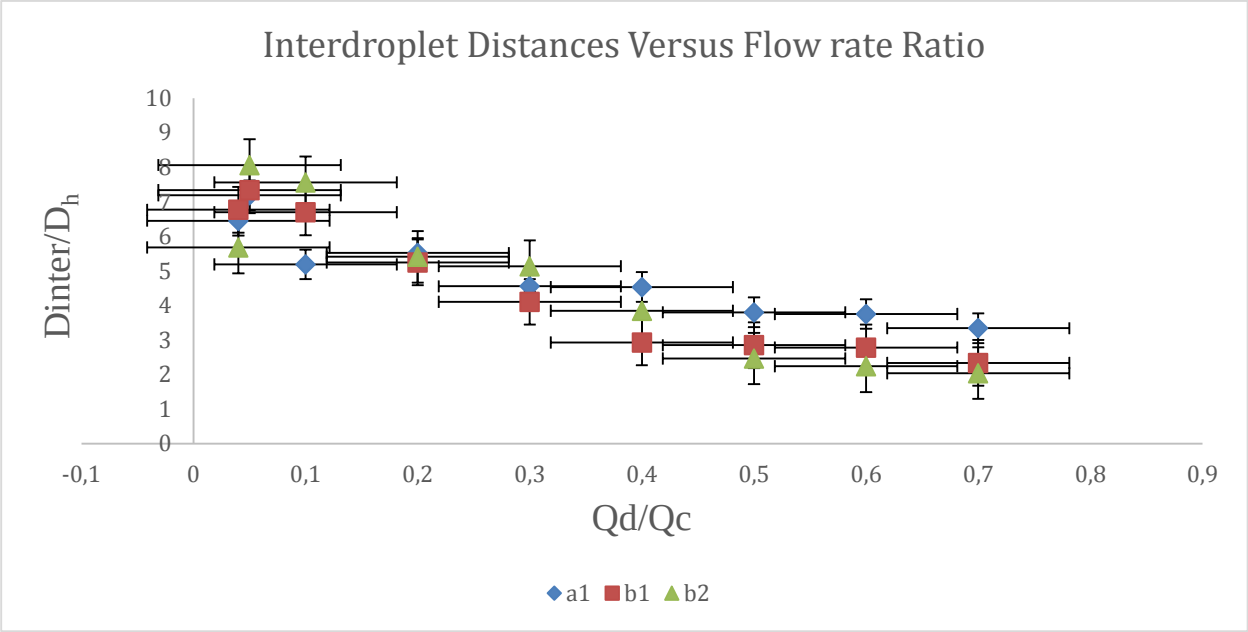

Figure 4. 2 Relationship between the average interdroplet distances and flow rate ratio (Qd/Qc): a1 shows the average interdroplet distances at the droplet generation junction, b1 shows the average interdroplet distances at the auxiliary junction and b2 shows the average interdroplet distances just before they entered the serpentine.

Figure 4.3 shows to what extent the droplet shrank from the initial size (a1) before getting to the serpentine (b2). It was observed that at the optimized flow ratio (about 0.1 µL/min), which corresponds to 0.005 (continuous to dispersed phase) about 30 % shrinkage in

diameter occurred from 105.23 ±5 µm diameter in a1 to 70 ±3 µm at b2 just before it enters the serpentine. Possible reasons for this situation were discovered to be the dissolution of DMF from the dispersed phase into the continuous phase. Because of this droplet shrinkage along the channel, the concentration of the micro-reactors/droplets formed from the precursor solution was changing as the droplet moved along the channels, and nucleation may start with a different concentration when the droplets get smaller. Possible reasons for this shrinkage were investigated and will be discussed fully in section 4.4.

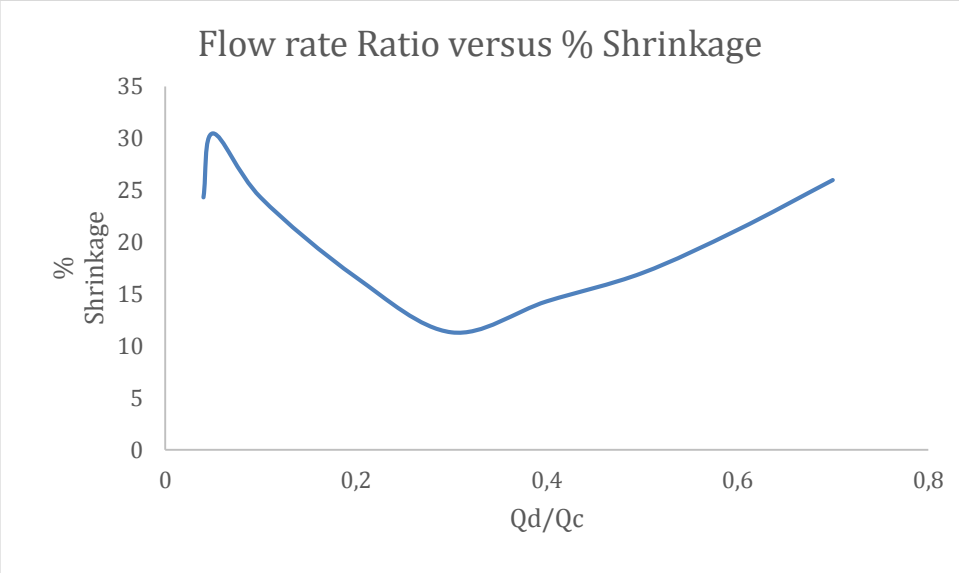

Figure 4. 3. Showing the relationship between flow rate ratio versus % shrinkage in diameter from the droplet formation region to the heating region.

4.1.2 Optimization of Droplet Generation in the Hot Region

Figure 4.4 shows how the droplet sizes reduced until nucleations were observed under a constant temperature (80 ^{o}C) but with different starting droplet sizes. For the 70 ±3 µm droplet sizes, the first nucleations were observed in the 5th serpentine, whereas nucleations were observed at the 13th and 16th serpentines for the 90 ±5 and 110 ±5 µm droplet sizes respectively. It can be seen from Figure 4.3 that nucleation took place earlier and the reduction was smoother for the smallest droplet size. therefore, it is better to work with relatively small droplet sizes. Also, while the 70 µm droplet shrank to 25 µm before nucleations were observed, the 90 and 110 µm droplets were slightly less at 23 and 22

µm respectively. This suggests that a smaller droplet size reaches enough supersaturation to nucleate earlier than a larger droplet size under the same synthetic condition.

Figure 4. 4. Progressive shrinkage in the size of droplets as they flow along the serpentine at the elevated temperature, 80 ^{o}C..

4.2 Crystallization of the Precursor Solution

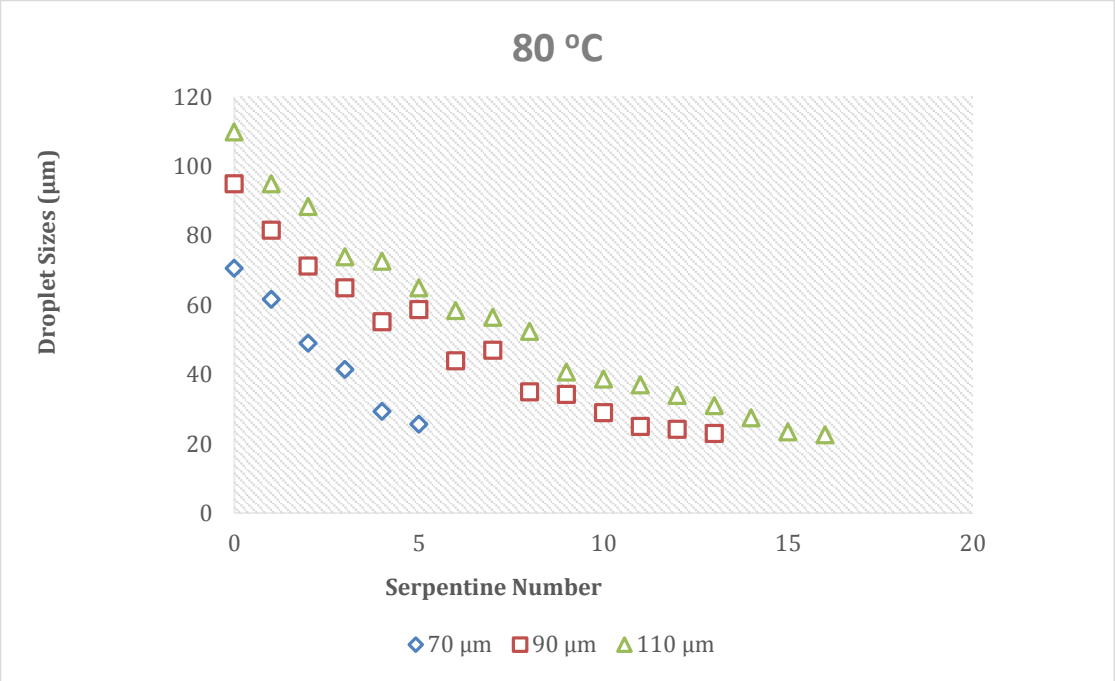

The precursor solution containing zirconium chloride and BDC (UiO-66 precursor solution) was crystallized at three different temperatures and three different droplet sizes. The times at which nucleation was first observed were recorded as the residence time.

4.2.1 Effect of Droplet Size on Crystallization of time of the Precursor Solution

As shown in figure 4.5, droplet size was found to have a direct relationship with the residence time as a larger droplet size took a longer residence time to nucleate. This phenomenon, i.e. the residence time for nucleation to take place in the serpentine based on the droplet volume is illustrated schematically in Figure 4.6. While it took about 30 ±5 seconds for 70 ±3 µm droplet size to nucleate, the first observable nucleation of the 90 ±5 and 110 ±5 µm took place at 109 ±3 and 112 ±5 seconds respectively. Surprisingly, the residence times for the 90 and 110 µm were quite close. It could be that due to the large size of the droplets they took longer times to reach enough supersaturation to nucleate and underwent instantaneous nucleation once supersaturation was reached. If this is the case, that agrees with the Lamer model of instantaneous nucleation. Alternatively, it could be a result of an error in noticing the point of nucleation as droplets have to be followed with eyes to determine the point of nucleation. Large droplets are often very fast and tend to move more randomly in the channels and the serpentine. As the droplets moved along the serpentine, they often caught up with each other and stuck together, especially when they passed through the U-turn. This could be a result of additional pressure encountered when passing through the U-turn, which tends to alter their speed.

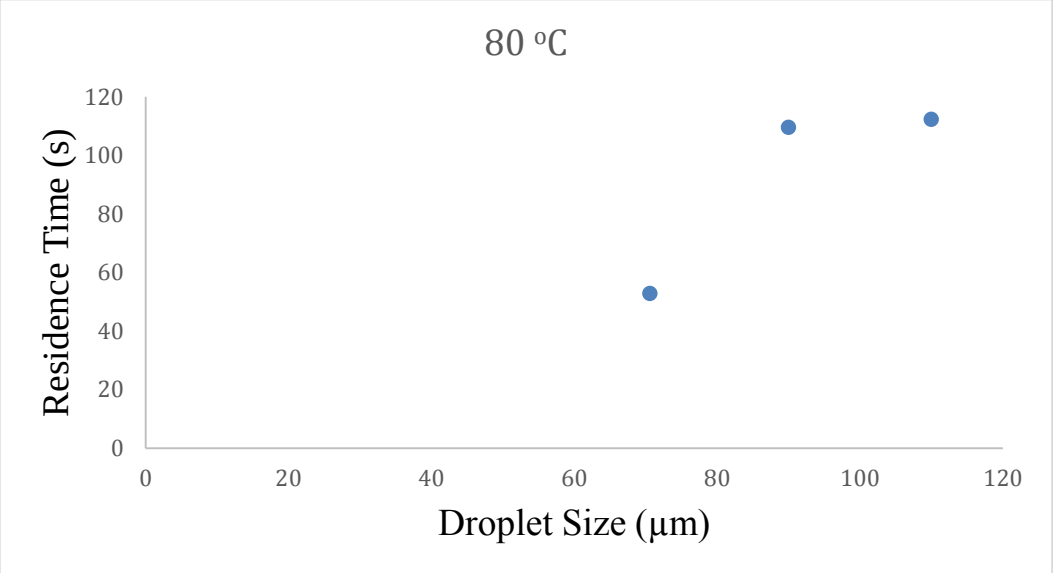

Figure 4. 5. The effect of the size of the droplets on the time untill nucleation in the UiO-66 precursor solution

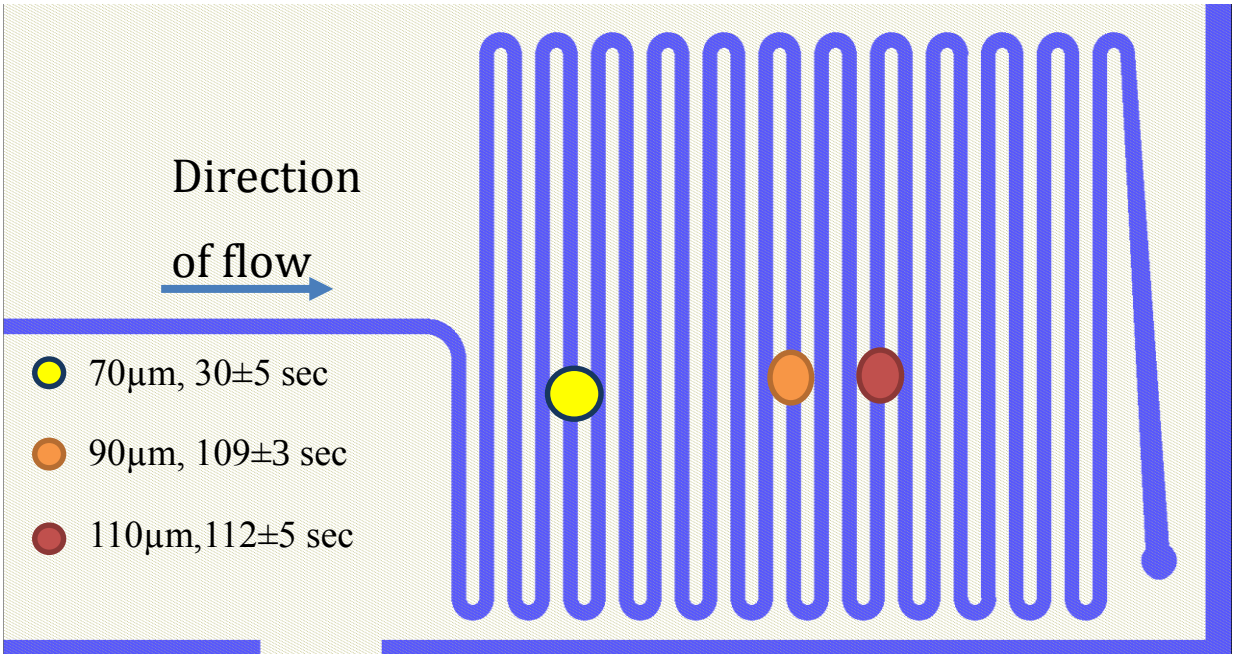

Figure 4. 6. Schematic diagram showing the serpentine where nucleations of UiO-66 precursor solution were first observed and the effect of droplet size on nucleation time.

4.2.2 Effect of Temperature on Crystallization of UiO-66 Precursor Solution

As shown in Figure 4.7, the temperature was found to have an inverse relationship with the residence time for nucleation to occur. An increase in temperature resulted in faster nucleation [45]. The 70 µm droplet size was chosen because it was the optimized condition with stable and relatively equal interdroplet distances. At 100 ^{o}C instantaneous nucleation was observed (just about 11 ±5 seconds), while it took 30 ±5 and 90 ±6 seconds to observe nucleations at 80 and 50 ^{o}C. These results agree with Lamer's instantaneous model of nucleation [49]. Higher temperatures may have led the solution to rapid generation of supersaturation to overcome the energy barrier required for reactions to take place. The change in concentration along the channel until nucleation took for the three temperatures under consideration are presented in Appendix 10-12.

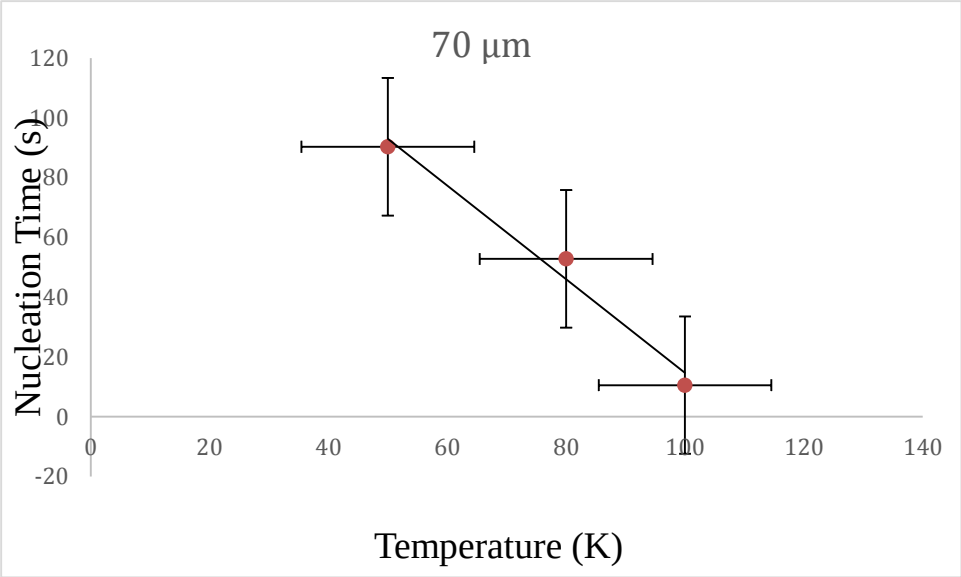

Figure 4. 7. The effect of temperature on the time until nucleation of the UiO-66 precursor solution

Figure 4. 8. Schematic representation of points of nucleation of UiO-66 precursor solution at different temperatures with their final diameters just before nucleations were

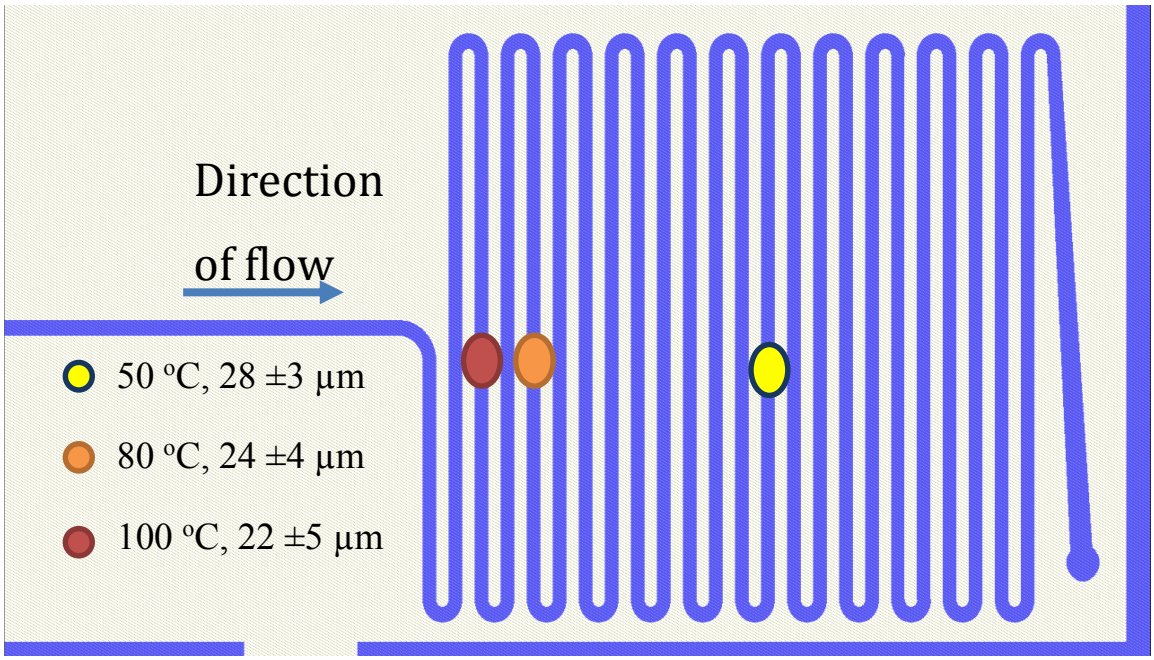

observed.

4.3 Kinetic Model Calculation

The kinetic parameters generated at different temperatures are presented in Table 4.1. The slope of the curve ($-1.64\,x\,10^9$) in Figure 4.9 was inserted into the CNT model (Equation 3.2) to represent the equation of the rate of nucleation of droplets in the microfluidic system used in this study (Equation 4.1).

$$\boldsymbol{J\,(s^{-1}) = k_N exp\left(\frac{-1.64\,x\,10^9}{T^3 \ln(S)^2}\right)} \quad (4.1)$$

Table 4.1 Nucleation Parameters

T (ºC)	Number of Droplets Counted	Number of Nucleated	Nucleation Time (s)	C.ZrCl4	C.BDC	C*ZrCl$_4$	C*BDC	Droplet Nucleation	lnJ	$\frac{1}{T^3(lnS)^2}$
50	71±9	26	90 ± 5	64.54732	122.3002	1008.551	1910.940	0.2878	-1.2417	-5.390E-09
80	103±20	55	30 ±5	64.54732	122.3002	1309.374	2480.919	1.8333	0.6061	-3.771E-09
100	140±15	63	11 ± 5	64.54732	122.3002	1475.160	2795.040	5.7272	1.7452	-3.075E-09

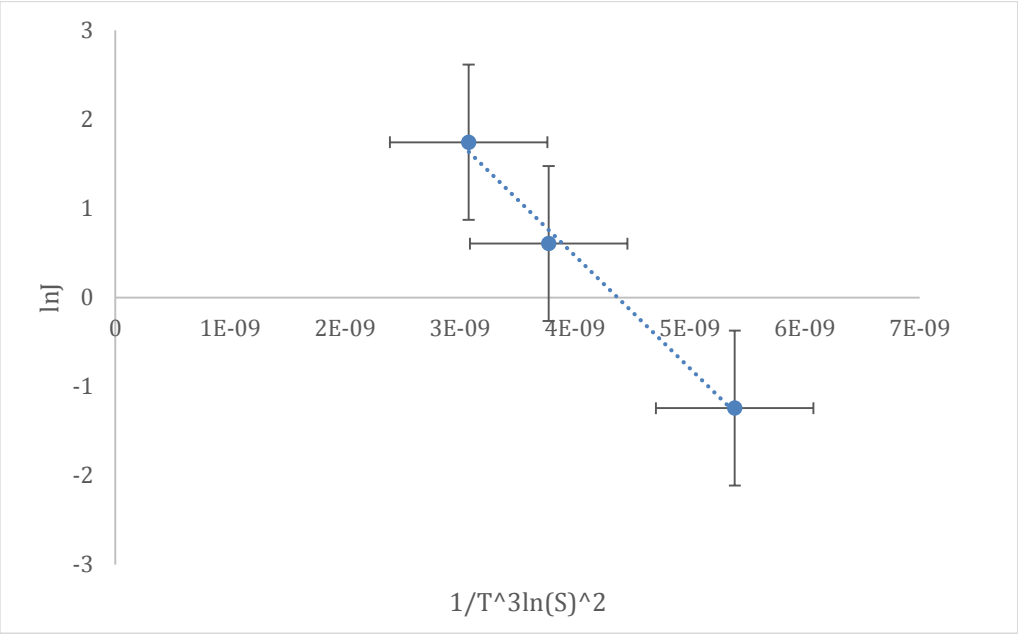

Figure 4.9 Rate of nucleation as a function of temperature and supersaturation ratio. The slope of this graph was inserted into equation 3.1 to model the nucleation rate in the microfluidic system.

The nucleation rate kinetic constant (k_N) calculated for each temperature using equation 4.1 showed a direct proportion with temperature. k_N values are 0.0003175 s^{-1}, 0.0156 s^{-1} and 0.1174 s^{-1} for 50, 80 and 100 ^oC, respectively. The increase in the rate constant with temperature shows that temperature leads to faster nucleation by generating enough supersaturation early to drive the nucleation phenomena. The activation energy barrier to overcome for nucleation to occur was calculated using the Arrhenius equation (equation 3.5) and presented in Table 4.2. The slope of the curve in Figure 4.10 was found as 119 $KJmol^{-1}$ and the intercept gave the constant k_o as 5.7969E+15 s^{-1}.

The values of the nucleation rate constants show the effect of increasing temperature on the rate of nucleation. At higher temperatures, nucleation takes place at a faster rate with a lower supersaturation ratio. The lowering of the supersaturation ratio by increasing temperature agrees with several crystallization studies in the literature [36, 56]. The calculated nucleation rate constants are also in agreement with the work of Bagi et.al [45], and the activation energy of 119 $KJmol^{-1}$ falls within the range estimated by Dombrowski et. al [56] and Schmitt et.al [79]

Table 4.2 Arrhenius Calculation Parameters

k_N (s^{-1})	lnk_N	1/T (K^{-1})
3.1756×10^{-4}	-7.7314	0.003094538
0.0156	-4.48295	0.002831658
0.1174	-1.95758	0.002679887

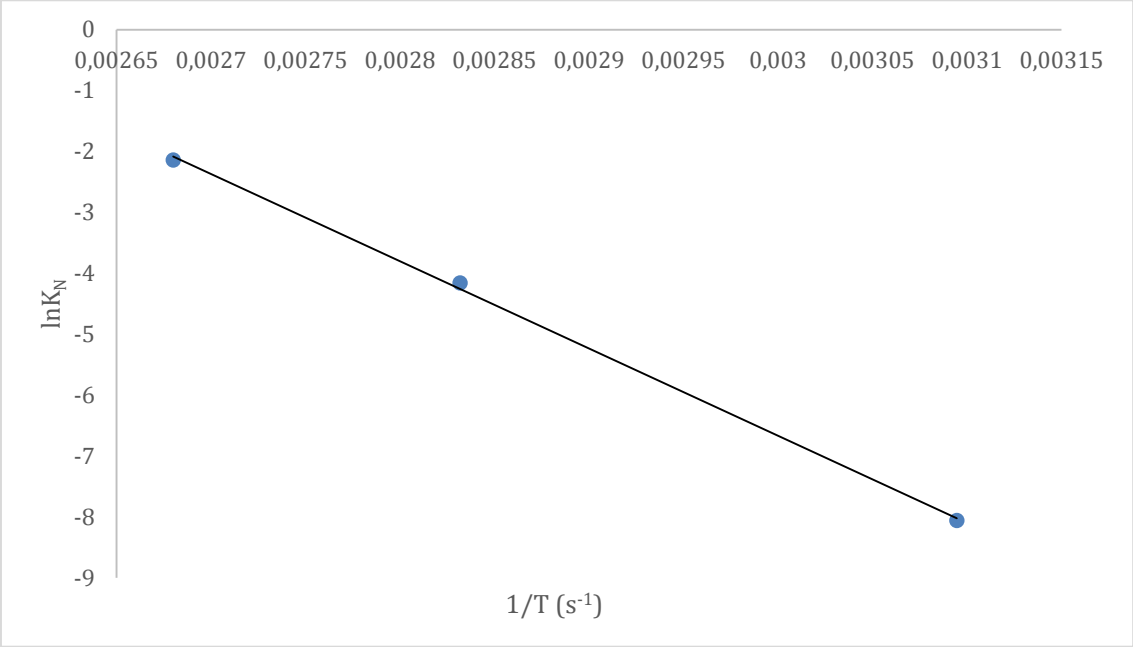

Figure 4.10 Plot of Nucleation kinetic rate constant (k_N) versus the inverse of temperature (1/T). The slope gives the activation energy from the Arrhenius equation.

The XRD results obtained for the synthesized crystals are shown in Figure 4.11. The blue pattern represents the synthesized crystals at 50 ^oC, while the red pattern was synthesized at 80 ^oC. The XRD pattern at both temperatures did not quite agree with the XRD patterns of UiO-66 crystals gotten from the literature [72]. However, it can be seen that the peaks in the 80 ^oC pattern were improved and some new crystalline peaks emerged. This shows that as temperature increases the crystallinity also increases, which agrees well with information gotten from the literature [72] as shown in Figure 4.12. The SEM (scanning electron microscope) image is shown in Appendix 9.

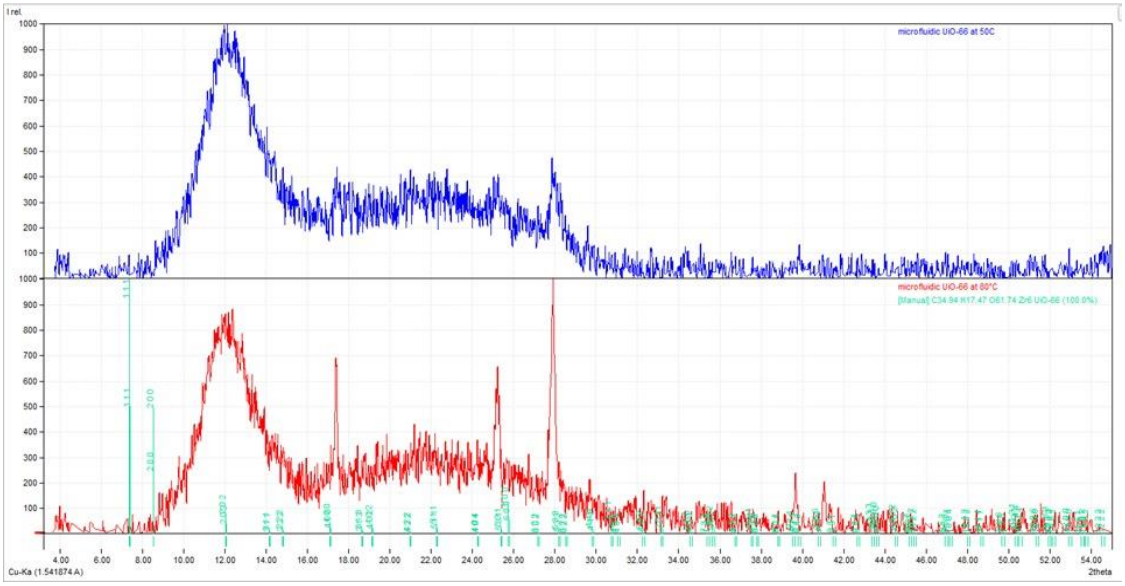

Figure 4. 11. XRD pattern obtained from crystallization of UiO-66 precursor solution: the blue pattern belongs to the particles synthesized at 50 ºC and the red pattern belongs to the particles synthesized at 80 ºC.

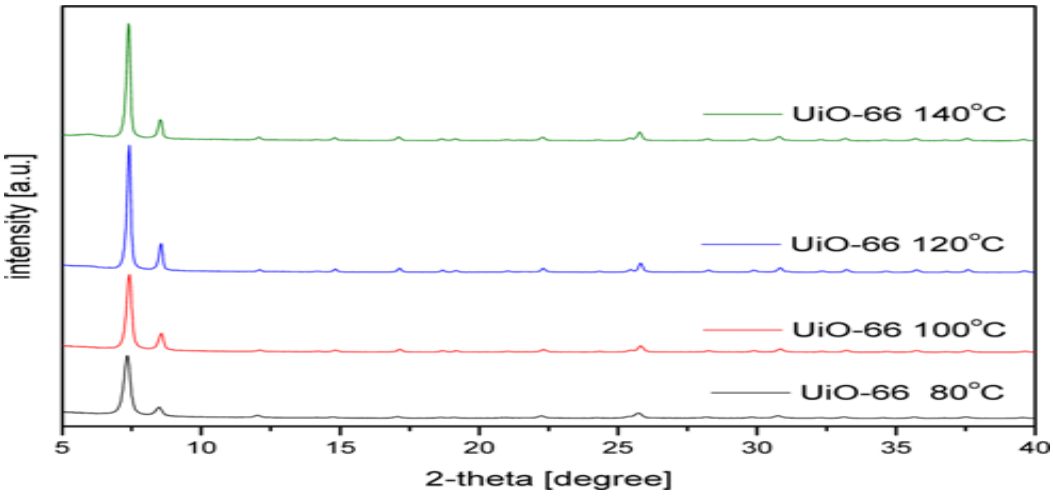

Figure 4.12. Effect of temperature on the crystallinity of UiO-66 MOF crystals found in the literature [72].

The XRD pattern showed an amorphous structure with some degree of crystallinity. Several reasons may be responsible for this. Since residence time, the concentration of reactants, the type of solvents, and pH used also have a strong influence on the crystallization behavior of MOFs [45], other parameters other than the ones captured in this work may be responsible. The shrinking of the droplets, which significantly increases the concentration of the dispersed phase even before heating was applied was investigated.

4.4 Investigation of Droplet Shrinkage in Silicone Oil

Since the droplets were observed to shrink during the optimization experiment even when the flow rates were not changed and since the XRD pattern of the obtained crystals did not come out as expected. It is desired to know if any of the components of the precursor solution was dissolving in oil which might alter the concentration. Firstly, a droplet formed by the precursor solution in silicone oil was observed on the glass slide. The variation of this droplet over time is given in Figure 4.13. As can be seen, as a result of the dissolution of a component in the precursor solution into silicone oil, the droplet shrank over time and a solid substance was observed inside. Since the precursor solution contains BDC ligand and $ZrCl_4$ salt, and DMF as the solvent, the shrinkage behavior of the droplets obtained from the BDC+DMF and $ZrCl_4$+DMF solutions and pure DMF solvent separately were analyzed to understand which of the components was passing into the oil.

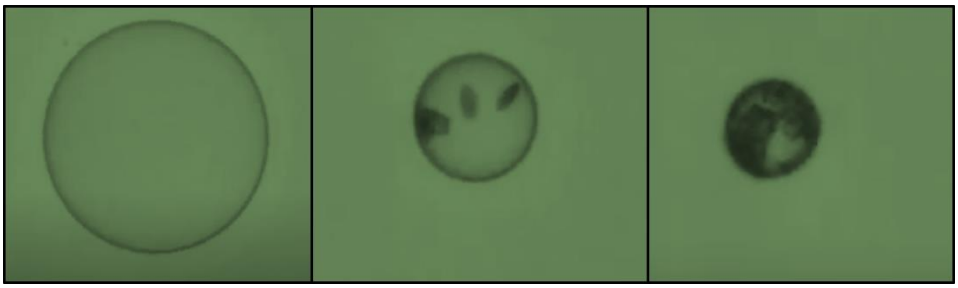

Figure 4.13: Shrinking behavior of the droplet formed by the precursor solution in the silicone oil.

The change over time of a droplet formed in silicone oil by the solution consisting of a mixture on the glass slide is given in Figure 4.14. As can be seen, only the BDC ligand, which was initially solid, remains due to the diffusion of DMF in the droplet into the oil over time. As a result of these experiments, it has been proven that the BDC ligand does not pass into the silicone oil.

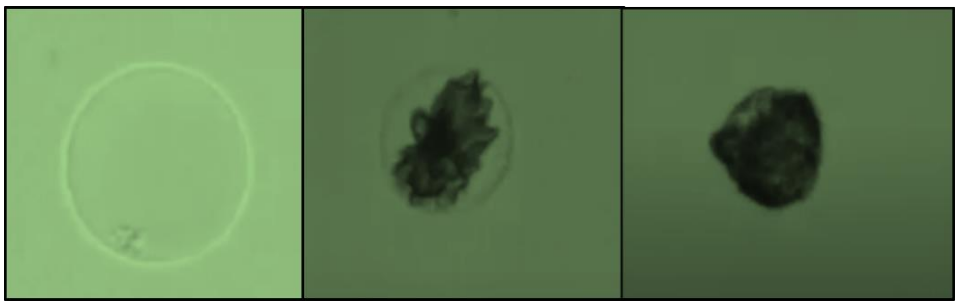

Figure 4.14. Shrinkage behavior of the droplet formed by the BDC+DMF solution in the silicone oil

Likewise, the change in the form of a droplet formed by $ZrCl_4$+DMF solution in silicone oil over time is shown in Figure 4.14. Again, after a certain time, it was seen that only a transparent solid structure remains due to the dissolution of DMF into the oil. As a result of these experiments, it was observed that $ZrCl_4$ was not dissolving into the silicone oil. As a result of all these observations, the idea that the reason for the shrinkage of the droplets obtained with the precursor solution was that the DMF in the solution was dissolving into the silicone oil became more convincible. To support this idea, the shrinkage behavior of the droplets formed in the silicone oil using pure DMF was observed.

Figure 4.15. Shrinkage behavior of droplet formed by $ZrCl_4$+DMF solution in silicone oil.

As seen in Figure 4.15, the pure DMF droplet shrank until it disappeared completely into the silicone oil. In light of these results, it was observed that the DMF solvent was dissolving in the silicone oil. This finding could also be one of the reasons the XRD pattern of the obtained crystal structure from the UiO-66 precursor solution did come out as expected.

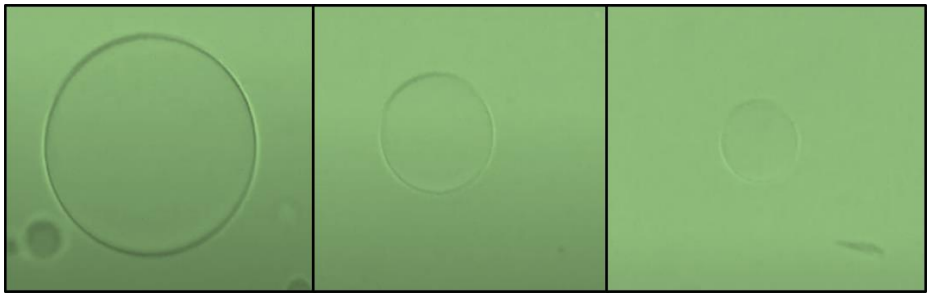

Figure 4.16. Shrinkage behavior of droplets formed by pure DMF in silicone oil.

5. CONCLUSIONS

In this work, optimization of droplet generation in a two-phase microfluidic system was carried out using UiO-66 precursor solution and silicone oil as the dispersed and continuous phases, respectively. The analyses of the flow conditions was divided into cold and hot regions. In the cold regions, as the ratio of both phases (Qd/Qc) reduced the droplet sizes reduced in a direct relationship and the interdroplet distances increased.
As the size of the droplets is reduced, they become more spherical, monodispersed, and flow at a relatively constant distance apart. It was observed that at flow rate ratio Qd/Qc of 0.05 corresponding to flow rates of 0.1 and 2 μL/min for the dispersed and continuous phases respectively, an average droplet size of 70 ±3 μm was achieved with a stable flow and relatively equal distance.

Analysis of the flow in the hot region shows that droplet sizes progressively reduced along the serpentine creating supersaturation until nucleation took place. At 80 ^{o}C while 70 μm nucleated at the 5th leg of the serpentine, those of 90 and 110 μm nucleated at the 13th and 16th legs of the serpentine, respectively. It was also observed that working with smaller droplet sizes as much as possible is better as large droplets move very fast in the channel, can catch up with each other and coalescence, and therefore, are difficult to control.

Crystallization experiments were carried out at three different temperatures and three different droplet sizes. Droplet sizes affected the nucleation time, with smaller droplets nucleating earlier than the larger droplet sizes.
Nucleation occurred earlier at higher temperatures as it took just 11 ±5 seconds to achieve nucleation for 100 ^{o}C while 90 ±6 and 30 ±5 seconds of nucleation time were observed at 80 ^{o}C and 50 ^{o}C, respectively.
The results obtained from the three nucleation temperatures were used in classical nucleation theory (CNT) to implement the calculation of the kinetic parameters for nucleations in the microfluidic system. Nucleation kinetic rate constant k_N increased from 0.0004388 s^{-1} for 50 ^{o}C to 0.0113 and 0.1412 s^{-1} for 80 ^{o}C and 100 ^{o}C, respectively. The activation energy for nucleation calculated from the slope of the linearized Arrhenius equation was 114 kJ while the intercept gave the Arrhenius constant k_o as 1.204E+15 s^{-1}.

Though the synthesized crystal does quite not match the XRD pattern from the literature, the effect of temperature was very clear as new peaks and existing ones improved at a higher temperature, confirming that high temperature fast track the generation of enough supersaturation for nucleation to take place early, which is sufficient for crystal growth. This agrees with the instantaneous nucleation model of Lamer. Other factors not outside the scope of this work might be responsible. Droplet shrinkage investigation was carried out and it was discovered that DMF which is the solvent for organic ligand (BDC) and metal salt ($ZrCl_4$) was passing into the oil phase as droplets progressed along the channels. Hence, an increase in the concentration of the precursor solution as the DMF dissolved into the oil phase is one of the main reasons.

Future works may include changing the concentrations of the three constituents of the precursor solution (DMF, HBDC, and $ZrCl_4$) to ensure enough DMF necessary for crystallization of UiO-66 nanoparticles remain in the solution till the end of the crystallization process, using other solvents such as ethanol and modulators such as hydrochloric acid (HCl) and redesign of the PDMS microfluidic device to extend the serpentine region which will enable the nucleated droplets sufficient time for crystal growth before exit.

6. REFERENCES

1. Niculescu, A.G., et al., *Nanomaterials Synthesis through Microfluidic Methods: An Updated Overview.* Nanomaterials (Basel), 2021. **11**(4).
2. Bally, F., et al., *Micromixer-assisted polymerization processes.* Chemical Engineering Science, 2011. **66**(7): p. 1449-1462.
3. Hwang, J., et al., *Microchannel Fabrication on Glass Materials for Microfluidic Devices.* International Journal of Precision Engineering and Manufacturing, 2019. **20**(3): p. 479-495.
4. Olanrewaju, A., et al., *Capillary microfluidics in microchannels: from microfluidic networks to capillaric circuits.* Lab Chip, 2018. **18**(16): p. 2323-2347.
5. Shrimal, P., G. Jadeja, and S. Patel, *A review on novel methodologies for drug nanoparticle preparation: Microfluidic approach.* Chemical Engineering Research and Design, 2020. **153**: p. 728-756.
6. Maeki, M., et al., *Microfluidic Approaches for Protein Crystal Structure Analysis.* Anal Sci, 2016. **32**(1): p. 3-9.
7. Cabeza, V.S., *High and Efficient Production of Nanomaterials by Microfluidic Reactor Approaches*, in *Advances in Microfluidics - New Applications in Biology, Energy, and Materials Sciences*. 2016.
8. Niculescu, A.G., et al., *Fabrication and Applications of Microfluidic Devices: A Review.* Int J Mol Sci, 2021. **22**(4).
9. Lai, X., et al., *Sticker Microfluidics: A Method for Fabrication of Customized Monolithic Microfluidics.* ACS Biomater Sci Eng, 2019. **5**(12): p. 6801-6810.
10. Song, Y., J. Hormes, and C.S. Kumar, *Microfluidic synthesis of nanomaterials.* Small, 2008. **4**(6): p. 698-711.
11. Yang, Q., Q. Xu, and H.L. Jiang, *Metal-organic frameworks meet metal nanoparticles: synergistic effect for enhanced catalysis.* Chem Soc Rev, 2017. **46**(15): p. 4774-4808.
12. Soni, S., P.K. Bajpai, and C. Arora, *A review on metal-organic framework: synthesis, properties and application.* Characterization and Application of Nanomaterials, 2018. **2**(2).
13. Huelsenbeck, L., et al., *Generalized Approach for Rapid Aqueous MOF Synthesis by Controlling Solution pH.* Crystal Growth & Design, 2020. **20**(10): p. 6787-6795.
14. Paz, F.A., et al., *Ligand design for functional metal-organic frameworks.* Chem Soc Rev, 2012. **41**(3): p. 1088-110.
15. Wang, Y., et al., *Continuous synthesis for zirconium metal-organic frameworks with high quality and productivity via microdroplet flow reaction.* Chinese Chemical Letters, 2018. **29**(6): p. 849-853.
16. Farha, O.K., et al., *De novo synthesis of a metal-organic framework material featuring ultrahigh surface area and gas storage capacities.* Nat Chem, 2010. **2**(11): p. 944-8.
17. Waitschat, S., M.T. Wharmby, and N. Stock, *Flow-synthesis of carboxylate and phosphonate based metal-organic frameworks under non-solvothermal reaction conditions.* Dalton Trans, 2015. **44**(24): p. 11235-40.

18. Cacho-Bailo, F., et al., *Metal-organic framework membranes on the inner-side of a polymeric hollow fiber by microfluidic synthesis.* Journal of Membrane Science, 2015. **476**: p. 277-285.
19. Ameloot, R., et al., *Interfacial synthesis of hollow metal-organic framework capsules demonstrating selective permeability.* Nat Chem, 2011. **3**(5): p. 382-7.
20. Arjmandi, M., et al., *Study of Separation Behavior of Activated and Non-Activated MOF-5 as Filler on MOF-based Mixed-Matrix Membranes in H2/CO2 Separation.* Petroleum Chemistry, 2018. **58**(4): p. 317-329.
21. Arjmandi, M., et al., *Influence of As-Formed Metal-Oxide in Non-Activated Water-Unstable Organometallic Framework Pores as Hydrolysis Delay Agent: Interplay Between Experiments and DFT Modeling.* Journal of Inorganic and Organometallic Polymers and Materials, 2018. **29**(1): p. 178-191.
22. Ha, J. and H.R. Moon, *Synthesis of MOF-on-MOF architectures in the context of interfacial lattice matching.* CrystEngComm, 2021. **23**(12): p. 2337-2354.
23. Ikigaki, K., et al., *MOF-on-MOF: Oriented Growth of Multiple Layered Thin Films of Metal-Organic Frameworks.* Angew Chem Int Ed Engl, 2019. **58**(21): p. 6886-6890.
24. Ma, Y., et al., *Formation of a thin and continuous MOF membrane with 2-D MOF nanosheets as seeds via layer-by-layer growth.* Chem Commun (Camb), 2019. **55**(68): p. 10146-10149.
25. Sim, J., et al., *Gas adsorption properties of highly porous metal-organic frameworks containing functionalized naphthalene dicarboxylate linkers.* Dalton Trans, 2014. **43**(48): p. 18017-24.
26. Lee, Y.-R., J. Kim, and W.-S. Ahn, *Synthesis of metal-organic frameworks: A mini review.* Korean Journal of Chemical Engineering, 2013. **30**(9): p. 1667-1680.
27. Raptopoulou, C.P., *Metal-Organic Frameworks: Synthetic Methods and Potential Applications.* Materials (Basel), 2021. **14**(2).
28. Zhang, B., et al., *Solvent determines the formation and properties of metal–organic frameworks.* RSC Advances, 2015. **5**(47): p. 37691-37696.
29. Leubner, S., et al., *Solvent Impact on the Properties of Benchmark Metal-Organic Frameworks: Acetonitrile-Based Synthesis of CAU-10, Ce-UiO-66, and Al-MIL-53.* Chemistry, 2020. **26**(17): p. 3877-3883.
30. Long, P., et al., *The Effect of pH on the Dimensionality of Coordination Polymers.* Inorganic Chemistry, 2001. **40**: p. 1271-1283.
31. Yassin, J.M., A.M. Taddesse, and M. Sánchez-Sánchez, *Room temperature synthesis of high-quality Ce(IV)-based MOFs in water.* Microporous and Mesoporous Materials, 2021. **324**.
32. Pedersen, J.F., et al., *Application of the single kernel wheat characterization technology to sorghum grain.* Cereal Chemistry, 1996. **73**(4): p. 421-423.
33. Li, S., et al., *Passive Picoinjection Enables Controlled Crystallization in a Droplet Microfluidic Device.* Small, 2017. **13**(41).
34. Alexander, F.I., S.M. Allan, and A. Stephen, *A statistical understanding of nucleation.* Journal of Crystal Growth, 1999. **196**: p. 234—242.
35. Teychene, S. and B. Biscans, *Microfluidic Device for the Crystallization of Organic Molecules in Organic Solvents.* Crystal Growth & Design, 2011. **11**(11): p. 4810-4818.
36. Teychene, S. and B. Biscans, *Crystal nucleation in a droplet based microfluidic crystallizer.* Chemical Engineering Science, 2012. **77**: p. 242-248.

37. Lingling, S., *Two-phase Flow in Micro and Nanofluidic Devices*, in *Institute for Nanotechnology* 2009, University of Twente, Enschede.
38. Song, H., D.L. Chen, and R.F. Ismagilov, *Reactions in droplets in microfluidic channels.* Angew Chem Int Ed Engl, 2006. **45**(44): p. 7336-56.
39. Utada, A.S., et al., *Monodisperse double emulsions generated from a microcapillary device.* Science, 2005. **308**(5721): p. 537-41.
40. Eijkel, J.C.T. and A.v.d. Berg, *Nanofluidics: what is it and what can we expect from it?* Microfluidics and Nanofluidics, 2005. **1**(3): p. 249-267.
41. Stone, H.A., A.D. Stroock, and A. Ajdari, *Engineering Flows in Small Devices: Microfluidics Toward a Lab-on-a-Chip.* Annual Review of Fluid Mechanics, 2004. **36**(1): p. 381-411.
42. Rossi, D., et al., *Adipic Acid Primary Nucleation Kinetics from Probability Distributions in Droplet-Based Systems under Stagnant and Flow Conditions.* Crystal Growth & Design, 2015. **15**(4): p. 1784-1791.
43. Zhang, S., et al., *Microfluidic platform for optimization of crystallization conditions.* Journal of Crystal Growth, 2017. **472**: p. 18-28.
44. Li, L., et al., *Microfluidic Control of Nucleation and Growth of CaCO3.* Crystal Growth & Design, 2018. **18**(8): p. 4528-4535.
45. Bagi, S.D., A.S. Myerson, and Y. Román-Leshkov, *Solvothermal Crystallization Kinetics and Control of Crystal Size Distribution of MOF-808 in a Continuous Flow Reactor.* Crystal Growth & Design, 2021. **21**(11): p. 6529-6536.
46. Coliaie, P., et al., *Patterned microfluidic devices for rapid screening of metal-organic frameworks yield insights into polymorphism and non-monotonic growth.* Lab Chip, 2022.
47. Shields, S.P., V.N. Richards, and W.E. Buhro, *Nucleation Control of Size and Dispersity in Aggregative Nanoparticle Growth. A Study of the Coarsening Kinetics of Thiolate-Capped Gold Nanocrystals.* Chemistry of Materials, 2010. **22**(10): p. 3212-3225.
48. Dunne, P.W., et al., *Continuous-flow hydrothermal synthesis for the production of inorganic nanomaterials.* Philos Trans A Math Phys Eng Sci, 2015. **373**(2057).
49. Whitehead, C.B., S. Özkar, and R.G. Finke, *LaMer's 1950 model of particle formation: a review and critical analysis of its classical nucleation and fluctuation theory basis, of competing models and mechanisms for phase-changes and particle formation, and then of its application to silver halide, semiconductor, metal, and metal-oxide nanoparticles.* Materials Advances, 2021. **2**(1): p. 186-235.
50. Bahrig, L., S.G. Hickey, and A. Eychmüller, *Mesocrystalline materials and the involvement of oriented attachment – a review.* CrystEngComm, 2014. **16**(40): p. 9408-9424.
51. Salmon, J.-B. and J. Leng, *Microfluidics for kinetic inspection of phase diagrams.* Comptes Rendus Chimie, 2009. **12**(1-2): p. 258-269.
52. Bourgeois, F., S. Teychené, and B. Biscans, *Applicability of Probabilistic Nucleation Modelling for the Analysis of Microfluidics Data.* KONA Powder and Particle Journal, 2018. **35**(0): p. 258-272.
53. Cavanaugh, J., M.L. Whittaker, and D. Joester, *Crystallization kinetics of amorphous calcium carbonate in confinement.* Chemical Science, 2019. **10**(19): p. 5039-5043.
54. Chen, K., et al., *Identification of nucleation rates in droplet-based microfluidic systems.* Chemical Engineering Science, 2012. **77**: p. 235-241.

55. Coliaie, P., et al., *Patterned microfluidic devices for rapid screening of metal-organic frameworks yield insights into polymorphism and non-monotonic growth.* Lab on a Chip, 2022. **22**(2): p. 211-224.
56. Dombrowski, R.D., et al., *Crystallization of alpha-lactose monohydrate in a drop-based microfluidic crystallizer.* Chemical Engineering Science, 2007. **62**(17): p. 4802-4810.
57. Ferreira, J., et al., *Protein crystallization in a droplet-based microfluidic device: Hydrodynamic analysis and study of the phase behaviour.* Chemical Engineering Science, 2018. **191**: p. 232-244.
58. Goh, L., et al., *A Stochastic Model for Nucleation Kinetics Determination in Droplet-Based Microfluidic Systems.* Crystal Growth & Design, 2010. **10**(6): p. 2515-2521.
59. Hong, D.H., et al., *MOF‐on‐MOF Architectures: Applications in Separation, Catalysis, and Sensing.* Bulletin of the Korean Chemical Society, 2021. **42**(7): p. 956-969.
60. Wang, X., et al., *MOFBOTS: Metal-Organic-Framework-Based Biomedical Microrobots.* Adv Mater, 2019. **31**(27): p. e1901592.
61. Akhavan-Sigari, R., et al., *Porous Cu-MOF nanostructures with anticancer properties prepared by a controllable ultrasound-assisted reverse micelle synthesis of Cu-MOF.* BMC Chem, 2022. **16**(1): p. 10.
62. Hu, G., et al., *Continuous and scalable fabrication of stable and biocompatible MOF@SiO2 nanoparticles for drug loading.* J Mater Chem B, 2018. **6**(47): p. 7936-7942.
63. Rohra, N., et al., *Microfluidic Synthesis of a Bioactive Metal-Organic Framework for Glucose-Responsive Insulin Delivery.* ACS Appl Mater Interfaces, 2022. **14**(6): p. 8251-8265.
64. Rafique, M.M., *Evaluation of Metal–Organic Frameworks as Potential Adsorbents for Solar Cooling Applications.* Applied System Innovation, 2020. **3**(2).
65. Butova, V.V., et al., *Metal-organic frameworks: structure, properties, methods of synthesis and characterization.* Russian Chemical Reviews, 2016. **85**(3): p. 280-307.
66. Anumah, A., et al., *Metal-Organic Frameworks (MOFs): Recent Advances in Synthetic Methodologies and Some Applications.* Chemical Methodologies, 2019. **3**(3): p. 283-305.
67. Jeong, G.-Y., et al., *Bioactive MIL-88A Framework Hollow Spheres via Interfacial Reaction In-Droplet Microfluidics for Enzyme and Nanoparticle Encapsulation.* Chemistry of Materials, 2015. **27**(23): p. 7903-7909.
68. Tanaka, Y., et al., *Competing Roles of Two Kinds of Ligand during Nonclassical Crystallization of Pillared-Layer Metal-Organic Frameworks Elucidated Using Microfluidic Systems.* Chemistry, 2020. **26**(41): p. 8889-8896.
69. Rubio-Martinez, M., et al., *Versatile, high quality and scalable continuous flow production of metal-organic frameworks.* Sci Rep, 2014. **4**: p. 5443.
70. Albrecht, R., *The Role of Hydrothermal Synthesis in Preparative Chemistry.* Angew. Chem. Int. Ed. Eng, 1985. **24**: p. 1026 - 1040.
71. Abdulraheem, A., et al., *Metal-Organic Frameworks (MOFs): Recent Advances in Synthetic Methodologies and Some Applications* Chemical Methodologies, 2019. **3**: p. 283-305.

72. Bae, S., et al., *Rapid solvothermal synthesis of microporous UiO-66 particles for carbon dioxide capture.* Korean Journal of Chemical Engineering, 2018. **35**(3): p. 764-769.
73. Son, W.J., et al., *Sonochemical synthesis of MOF-5.* Chem Commun (Camb), 2008(47): p. 6336-8.
74. Jung, D.W., et al., *Facile synthesis of MOF-177 by a sonochemical method using 1-methyl-2-pyrrolidinone as a solvent.* Dalton Trans, 2010. **39**(11): p. 2883-7.
75. Martinez Joaristi, A., et al., *Electrochemical Synthesis of Some Archetypical Zn2+, Cu2+, and Al3+ Metal Organic Frameworks.* Crystal Growth & Design, 2012. **12**(7): p. 3489-3498.
76. Bahar, Ö., *Optimization Of Two-Phase Flow Operating Parameters For Making Droplets In Microchannel Devices*, in *Department of Chemical Engineering*. 2021, Hacettepe University.
77. Anıl, H., *Investigation Of The Permeability Of The Cell Membrane For Different Cryoprotectant Agents In A Continuous Thermo-Fluidic Micro-Channel System*, in *Graduate School Of Natural And Applied Sciences*. 2021, Middle East Technical University, Ankara.
78. Bagi, S., et al., *Accelerated Synthesis of a Ni2Cl2(BTDD) Metal–Organic Framework in a Continuous Flow Reactor for Atmospheric Water Capture.* ACS Sustainable Chemistry & Engineering, 2021. **9**(11): p. 3996-4003.
79. Schmitt, E.A., D. Law, and G.G. Zhang, *Nucleation and crystallization kinetics of hydrated amorphous lactose above the glass transition temperature.* J Pharm Sci, 1999. **88**(3): p. 291-6.

APPENDIX

Appendix 1 – Detailed Calculation of Kinetic parameters

The classical nucleation theory gives the rate of nucleation from supersaturated solution as:

$$J\ (s^{-1})\ = k_N \exp\left(\frac{-16\pi\gamma^3 V_m^2}{3(KT)^3(lnS)^2}\right) \qquad (1)$$

where J is the rate of nucleation (s^{-1}), γ is the interfacial tension between the crystal and solution (N/m), V_m is the molecular volume of the crystallizing molecule (m^3/mol), k is the Boltzmann's constant (1.38 x 10^{-23} JK^{-1}), and T is the absolute temperature (K). S is the relative supersaturation ratio:

$$S\ = \frac{C}{C^*} \qquad (3)$$

where k_N is a kinetic constant of nucleation and is taken to have Arrhenius temperature dependency as shown below:

$$k_N(T) = \ k_0 \exp\left(-\frac{E_N}{RT}\right) \qquad (4)$$

From eq (1)

$$lnJ = lnk_N - \left(\frac{16\pi V_m^2\,\gamma^3}{3k^3}\,\frac{1}{T^3(lnS)^2}\right)$$

lnJ was plotted against $\frac{1}{T^3(lnS)^2}$ (Figure 4.9)

Slope = $\frac{16\pi V_m^2\,\gamma^3}{3k^3}$ = 1.264E+09

$\gamma^3 = 9.3921\ x\ 10^{-56}$

Surface tension $\gamma = 4.5456\ x\ 10^{-19}\ N/m$

$$\boldsymbol{J\ (s^{-1}) = \ k_N exp\left(\frac{-1.264\ x\ 10^9}{T^3 \ln(S)^2}\right)} \qquad ***$$

At 50 °C

$$0.2889 = \ k_N exp\left(\frac{-1.264\ x\ 10^9}{323.15^3\ \text{x2}\ \ln\left(\frac{64.5473}{1008.5518}\right)}\right)$$

$$\boldsymbol{k_N = 3.1756\ x\ 10^{-4}\ s^{-1}}$$

At 80 ^{o}C

$$1.8333 = k_N exp\left(\frac{-1.264\ x\ 10^9}{353.15^3\ \text{x2}\ \ln\left(\frac{64.5473}{1309.374}\right)}\right)$$

$$\boldsymbol{k_N = 0.0156\ \ s^{-1}}$$

At 100 ^{o}C

$$5.7272 = k_N exp\left(\frac{-1.264\ x\ 10^9}{373.15^3\ \text{x2}\ \ln\left(\frac{64.5473}{1475.16}\right)}\right)$$

$$\boldsymbol{k_N = 0.1174\ s^{-1}}$$

From equation 2

$$lnk_N(T) = lnk_0 - \frac{E_N}{R} * \frac{1}{T}$$

From table 4.2, lnk_N was plotted against $\frac{1}{T}$ (Figure 4.10)

Slope = $\frac{E_N}{R} = 14320.77577$

$$E_N = 14320.77577\ x\ 8.3145 = 119070.1 KJmol^{-1}$$

$$\boldsymbol{E_N = 119\ KJmol^{-1}}$$

$$\boldsymbol{k_0 = 5.7969E + 15}$$

Appendix 2- Microfluidic Two-Phase Flow Optimization Results

The raw data collected from the optimization experiment in the cold region of the microfluidic device.

S/No	Auxiliary Oil(QA) µL/min	Dispersed Phase (Qd) µL/min	Continuous Phase (Qc) µL/min	Qd/Qc	Droplet Size (µm) a1	Interdroplet Distance (µm) a1	Droplet Size (µm) b1	Interroplet Distance (µm) b1	Droplet Size (µm) b2	Interdroplet Distance (µm) b2	D*droplet, a1	D*interdroplet, a1	D*droplet, b1	D*interdroplet, b1	D*droplet, b2	D*interdroplet, b2	Di/Df	%Shrinkage
1	2	2	2	1														
2	2	1.8	2	0.9														
3	2	1.6	2	0.8														
4	2	1.4	2	0.7	230.45	445.5	191.77	374	170.55	326.4	1.728375	3.34125	1.1985417	2.3375	1.0659375	2.04	0.7401	25.992623
5	2	1.2	2	0.6	209	500.5	174.17	445.5	164.725	358.64	1.5675	3.75375	1.0885417	2.784375	1.0295313	2.2415	0.7882	21.184211
6	2	1	2	0.5	179.74	507.1	162.77	456.05	149.13	394.4	1.34805	3.80325	1.0173125	2.8503125	0.9320833	2.465	0.8297	17.0283
7	2	0.8	2	0.4	166.32	604.4	151.36	468.6	142.53	615.52	1.2474	4.533	0.946	2.92875	0.8908125	3.847	0.857	14.303752
8	2	0.6	2	0.3	155.47	607.2	143.55	656.7	137.87	821.7	1.166	4.534	0.8971875	4.104375	0.8616667	5.135625	0.8868	11.320755
9	2	0.4	2	0.2	137.87	735.9	128.26	839.3	114.95	865.43	1.034	5.51925	0.8016625	5.245625	0.7184375	5.4089375	0.8338	16.62234
10	2	0.2	2	0.1	119.17	691.9	109.45	1071.4	90.2	1210.2	0.89375	5.18925	0.6940625	6.69625	0.56375	7.56375	0.7569	24.307692
11	2	0.1	2	0.05	105.23	958.1	91.3	1173.7	73.15	1290.3	0.78925	7.18575	0.570625	7.335625	0.4571875	8.064375	0.6951	30.487805
12	2	0.08	2	0.04	94.97	860.1	80.67	1083	71.87	908.6	0.71225	6.45075	0.5041667	6.76875	0.4491667	5.67875	0.7568	24.324324

Appendix 3– Table of Values for calculating the residence time at 70 µm and 80 ºC

Channel	Serpentine distance (cm)	Time(s)	Velocity (cm/s)	Droplet size	Mean Velocity (cm/s)	Distance to Crystallization Point (cm)	Mean Time (s)
0	0.088334943	0.4	0.220837358	70.6	0.220527	6.57	29.79231956
1	0.088334943	0.40	0.211499045	61.66667			
2	0.088334943	0.33	0.209071667	49			
3	0.088334943	0.4	0.184294344	41.5			
4	0.088334943	0.4	0.26262356	29.33333			
5	0.088334943	0.4	0.23483384	25.66667			

The residence time was calculated by dividing the mean velocity of the droplets as they travelled along the serpentines by the distance covered until nucleation took place at the 5th serpentine.

Appendix 4 – Table of Values for calculating the residence time at 90 µm and 80 ºC

Channel	Serpentine Distance (cm)	Time(s)	Velocity (cm/s)	Droplet Size	Mean Velocity (cm/s)	Distance to Crystallization Point (cm)	Mean (s)
0	0.0430661	0.4	0.107665	95	0.173169	18.98	109.6039378
1	0.112174007	0.4	0.280435	81.66667			
2	0.06020465	0.4	0.150512	71.33333			
3	0.061742725	0.4	0.154357	65			
4	0.042409122	0.333333333	0.127227	55.25			
5	0.048998675	0.4	0.122497	58.75			
6	0.046801425	0.333333333	0.140404	44			
7	0.054272075	0.333333333	0.162816	47			
8	0.047240875	0.333333333	0.141723	35			
9	0.059215888	0.4	0.14804	34.25			
10	0.057239461	0.4	0.143099	29			
11	0.060753963	0.333333333	0.182262	25			
12	0.089539036	0.4	0.223848	24.25			
13	0.113160572	0.333333333	0.339482	23			

The residence time was calculated by dividing the mean velocity of the droplets as they travelled along the serpentines by the distance covered until nucleation took place at the 13th serpentine.

Appendix 5 - Table of Values for calculating the residence time at 110 µm and 80 ºC

Channel	Serpentine Distance	Time(s)	velocity (cm/s)	Droplet Size (µm)	Mean Velocity (cm/s)	Total Distance (cm)	Mean Residence Time (s)
0	0.059655338	0.333333333	0.178966013	110	0.207897	23.36	112.363503
1	0.056579188	0.333333333	0.169737563	95			
2	0.056260586	0.333333333	0.168781759	88.5			
3	0.10426171	0.4	0.260654274	74			
4	0.066911756	0.4	0.167279389	72.66667			
5	0.0694331	0.4	0.17358275	65			
6	0.06459915	0.4	0.161497875	58.5			
7	0.056603357	0.4	0.141508393	56.5			
8	0.078662649	0.333333333	0.235987946	52.5			
9	0.092625074	0.4	0.231562684	40.75			
10	0.079217454	0.4	0.198043636	38.66667			
11	0.095365045	0.4	0.238412611	37			
12	0.088550274	0.4	0.221375684	34			
13	0.105687725	0.4	0.264219313	31			
14	0.105138413	0.4	0.262846031	27.5			
15	0.087452747	0.333333333	0.262358242	23.5			
16	0.065809835	0.333333333	0.197429504	22.66667			

The residence time was calculated by dividing the mean velocity of the droplets as they travelled along the serpentines by the distance covered until nucleation took place at the 16th serpentine.

Appendix 6 - Table of Values for calculating the residence time at 70 µm and 50 ºC

Channel	Serpentine Distance (cm)	Time(s)	Velocity (cm/s)	Droplet Size	Mean Velocity (cm/s)	Distance to Crytalization point	Mean Residance Time (s)	Residance Time (min) heating
0	0.06273478	0.266667	0.235255	70	0.226287	20.44	90.32783	1.5054638
1	0.08734288	0.4	0.218357	66.66667				
2	0.06998241	0.333333	0.209947	61.33333				
3	0.07613471	0.4	0.190337	58.33333				
4	0.08195743	0.40	0.204894	55.33333				
5	0.08811082	0.40	0.220277	45.5				
6	0.0861322	0.40	0.215331	44.33333				
7	0.08734069	0.4	0.218352	41.33333				
8	0.08657604	0.40	0.21644	38.66667				
9	0.07360788	0.33	0.220824	34.5				
10	0.09075631	0.40	0.226891	33				
11	0.09162533	0.40	0.229063	31				
12	0.09284809	0.40	0.23212	30.5				
13	0.09261409	0.40	0.231535	29.5				
14	0.10822665	0.33	0.32468	28				

The residence time was calculated by dividing the mean velocity of the droplets as they travelled along the serpentines by the distance covered until nucleation took place at the 14th serpentine.

Appendix 7- Table of Values for calculating the residence time at 70 µm and 80 ºC

Channel	Serpentine Distance (cm)	Time(s)	Velocity (cm/s)	Droplet size (µm)	Mean Velocity (cm/s)	Distance to Crystallization Point (cm)	Mean Residence Time (s)
0	0.088334943	0.4	0.220837	70.6	0.220526636	6.57	29.79231956
1	0.084599618	0.40	0.211499	61.66667			
2	0.06899365	0.33	0.209072	49			
3	0.073717738	0.4	0.184294	41.5			
4	0.105049424	0.4	0.262624	29.33333			
5	0.093933536	0.4	0.234834	25.66667			

The residence time was calculated by dividing the mean velocity of the droplets as they travelled along the serpentines by the distance covered until nucleation took place at the 5th serpentine.

Appendix 8 - Table of Values for calculating the residence time at 70 µm and 100 ºC

Serpentine Distance (cm)	Time(s)	Velocity (cm/s)	Droplet size (µm)	Mean Velocity (cm/s)	Distance to Crystallization Point (cm)	Mean Residence Time (s)
0.09799735	0.33	0.293992	70	0.220527	2.92	10.63349152
0.10667868	0.4	0.266697	31			
0.10524937	0.4	0.263123	24.666667			

The residence time was calculated by dividing the mean velocity of the droplets as they travelled along the serpentines by the distance covered until nucleation took place at the 3rd serpentine.

Appendix 9 – SEM Image for crystallization at 80 ºC and 70 µm Droplet Size

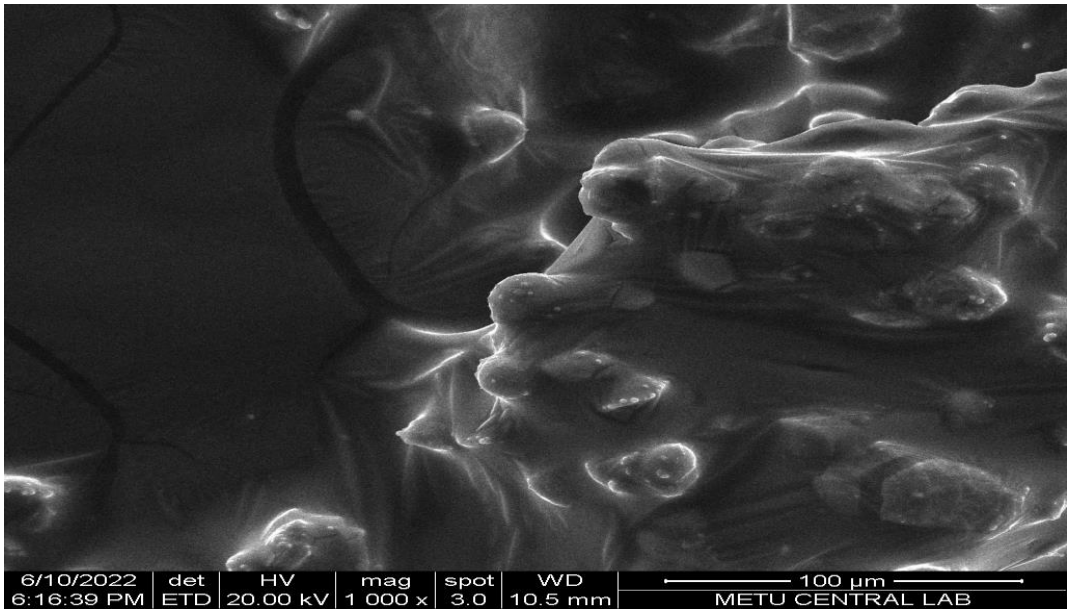

Appendix 10- Table Showing the Change in area, volume, and concentration at 50 ^{o}C and 70 µm droplet size

Region	Diameter (µm)	Area (µm2)	Area (m2)	Volume µm3	Volume (mL)	ZrCl4	H2BDC
a1	105.23	34792.47	3.47925E-08	610202.02	6.10202E-07	19	36
b1	91.3	26190.74	2.61907E-08	398535.73	3.98536E-07	29.09108904	55.1199582
b2	70	15395.8	1.53958E-08	179617.67	1.79618E-07	64.54731658	122.300179
1	66.66667	13964.44	1.39644E-08	155160.49	1.5516E-07	74.72158736	141.577744
2	61.33333	11819.51	1.18195E-08	120821.61	1.20822E-07	95.95831367	181.815752
3	58.33333	10691.53	1.06915E-08	103945.41	1.03945E-07	111.5377631	211.334709
4	55.33333	9620.106	9.62011E-09	88718.753	8.87188E-08	130.6808083	247.605742
5	45.5	6504.726	6.50473E-09	49327.502	4.93275E-08	235.0380212	445.335198
6	44.33333	6175.426	6.17543E-09	45629.54	4.56295E-08	254.086244	481.426568
7	41.33333	5367.932	5.36793E-09	36979.09	3.69791E-08	313.5241657	594.045788
8	38.66667	4697.639	4.69764E-09	30273.674	3.02737E-08	382.9676666	725.622947
9	34.5	3739.766	3.73977E-09	21503.652	2.15037E-08	539.1567254	1021.56011
10	33	3421.638	3.42164E-09	18819.009	1.8819E-08	616.0706121	1167.29169
11	31	3019.462	3.01946E-09	15600.554	1.56006E-08	743.1683927	1408.10853
12	30.5	2922.846	2.92285E-09	14857.798	1.48578E-08	780.3201004	1478.50124
13	29.5	2734.326	2.73433E-09	13443.767	1.34438E-08	862.3950681	1634.01171
14	28	2463.328	2.46333E-09	11495.531	1.14955E-08	1008.551822	1910.94029

This table shows the change in volume, area and concentration of precursor solution from the droplet generation to the point of nucleation.

Appendix 11- Table Showing the Change in area, volume, and concentration at 80 ºC and 70 µm droplet size

Region	Diameter (µm)	Area (µm2)	Area (m2)	Volume (µm3)	Volume (mL)	ZrCl4 (mM)	H2BDC (mM)
a1	105.23	34792.47	3.47925E-08	610202.0207	6.10202E-07	19	36
b1	91.3	26190.74	2.61907E-08	398535.7296	3.98536E-07	29.09109	55.11995818
b2	70	15395.8	1.53958E-08	179617.6667	1.79618E-07	64.54732	122.3001788
1	61.66667	11948.33	1.19483E-08	122802.2776	1.22802E-07	94.41061	178.8832681
2	49	7543.942	7.54394E-09	61608.85967	6.16089E-08	188.1846	356.560288
3	41.5	5411.31	5.41131E-09	37428.22404	3.74282E-08	309.7619	586.9173147
4	29.3333	2703.51	2.70351E-09	13217.14645	1.32171E-08	877.1817	1662.028399
5	25.66667	2069.88	2.06988E-09	8854.489166	8.85449E-09	1309.374	2480.919264

This table shows the change in volume, area and concentration of precursor solution from the droplet generation to the point of nucleation.

Appendix 12- Table Showing the Change in area, volume and concentration at 100 ^{o}C and 70 µm droplet size

Region	Diameter (µm)	Area (µm2)	Area (m2)	Volume (µm3)	Volume (mL)	ZrCl4 (mM)	H2BDC (mM)
a1	105.23	34792.47	3.47925E-08	610202.021	6.10202E-07	19	36
b1	91.3	26190.74	2.61907E-08	398535.73	3.98536E-07	29.09109	55.11996
b2	70	15395.8	1.53958E-08	179617.667	1.79618E-07	64.54732	122.3002
1	31	3019.462	3.01946E-09	15600.5537	1.56006E-08	743.1684	1408.109
2	24.6667	1911.738	1.91174E-09	7859.37636	7.85938E-09	1475.16	2795.04

This table shows the change in volume, area and concentration of precursor solution from the droplet generation to the point of nucleation.